8-2017

Observation and estimation study for sensorless control of linear vapor compressors.

Joseph Latham
University of Louisville

OBSERVATION AND ESTIMATION STUDY FOR SENSORLESS
CONTROL OF LINEAR VAPOR COMPRESSORS

By

Joseph Latham
B.S., Western Kentucky University, 2012
M.S., University of Louisville, 2014

A Dissertation
Submitted to the Faculty of the
J.B. Speed School of Engineering of the University of Louisville
in Partial Fulfillment of the Requirements
for the Degree of

Doctor of Philosophy
in Electrical Engineering

Department of Electrical and Computer Engineering
University of Louisville
Louisville, Kentucky

August 2017

OBSERVATION AND ESTIMATION STUDY FOR SENSORLESS CONTROL OF LINEAR VAPOR COMPRESSORS

By

Joseph Latham
B.S., Western Kentucky University, 2012
M.S., University of Louisville, 2014

A Dissertation Approved on

July 14, 2017

by the following Dissertation Committee:

_____
Michael McIntyre, Dissertation Director

_____
John Naber

_____
Tamer Inanc

_____
Chris Richards

ABSTRACT

OBSERVATION AND ESTIMATION STUDY FOR SENSORLESS CONTROL OF LINEAR VAPOR
COMPRESSORS

Joseph Latham

July 14, 2017

Linear vapor compressors have become widely investigated for refrigeration applications due to their high efficiency in comparison to the more common rotary type compressors. However, the nature of the linear compressor adds complexity to the control of these machines. The unconstrained motion of the piston in a linear compressor allows for continuous modulation of the compressor output, but requires knowledge of the mechanical dynamics to effectively control the compressor and prevent collision of the piston with the cylinder head. This control is made more difficult by the highly nonlinear nature of the force of gas compression acting against the piston. As this gas force changes so does the resonant frequency of the system. Efficient control of the compressor requires knowledge and tracking of this resonant frequency in addition to other objectives. Sensorless control of the system is preferred for reliability, ease of production, and cost effectiveness. To this end a series of nonlinear observers and a combination of controllers have been developed for the linear vapor compressor.

TABLE OF CONTENTS

LIST OF FIGURES

1   INTRODUCTION

Rising energy costs and environmentally motivated legislation has led to increased research and development in the area of high efficiency domestic appliances. In the realm of refrigeration this has resulted in a renewed interest in linear vapor compressors over the historically more common rotary type. Linear compressors offer a gain in efficiency over the rotary compressor due to the fact that the motor force is inherently linear and therefore requires no mechanical conversion to actuate the piston [1]. Along with other factors this has allowed linear compressors to demonstrate improvements in efficiency of 10-20% over that of traditional rotary compressors driven by induction motors [2].

Despite these gains in efficiency there is an increase in complexity in the use of a linear compressor over a rotary device. Whereas in a rotary compressor the piston stroke (peak-to-peak displacement) is defined and constrained by the diameter of rotation, in a linear compressor the piston is free, allowing the stroke to be variable. This is an advantage in that it allows for the modulation of the compressor output, however it adds complexity in that the force of gas compression is free to change the piston's path. These effects necessitate an additional level of control to achieve efficient and stable operation of a linear compressor [3]. This control necessitates knowledge of the piston dynamics, which could most directly be obtained through use of some type of sensor as in [4], [5]. However, due to the extreme environment in a refrigerator compressor, i.e. refrigerant and oil, it is not cost effective to place a sensor inside the compressor. Moreover, the shell is hermetically sealed and if a sensor is to be used, at least two additional wires are required to penetrate the shell, which may not be acceptable in production. Hence sensorless control of the piston is generally preferred [6].

Efforts in this space include an external self-sensor circuit which utilizes voltage and current measurements to create a position signal [7] as well as algorithms such as those presented in [6], [8], [9], [10] which utilize the same signals to arrive at a position signal computationally. However, each of these methods has one or more significant weaknesses. For instance, [6] requires the taking of numerical

1

derivatives which amplifies the noise present in measured signals. The methods in [6], [8], and [9] require integration of signals which, due to unavoidable biases in voltage detection circuits, may become unbounded. In [10] this problem is addressed and is avoided by utilizing a high-pass filter to eliminate any DC bias in the velocity signal being integrated. However, since the real position signal has a significant DC component which varies with the force of gas compression, this method is incapable of accurately estimating this component and thus the absolute position.

Control of a linear compressor typically consists of two main objectives; resonance control to ensure maximum efficiency and stroke control to prevent collision and modulate output. Resonance control requires identification and tracking of the system resonant frequency which changes with gas force. In [11] this tracking is achieved using a perturb and observe algorithm to search for the maximum power point. The nature of this algorithm results in 'hunting' or undesirable oscillation in the frequency. In [12] the resonant frequency is calculated directly from the system mechanical dynamics, but requires a linearization of the gas force, which is not accurate, or at least very limited given that gas force is highly nonlinear. A method was developed for identifying resonance via the relative phase between motor current and piston position in [13] and similarly between current and velocity in [14], [15]. Both of these methods require signals which must be estimated if the methods are to be implemented sensorlessly. A current controller has been designed using a hybrid proportional-integral/neural network controller a sinusoidal current trajectory once the resonant frequency has been identified [16].

The second objective is control of the top dead center position, which corresponds to the minimum distance between the piston and the cylinder head. The purpose of this control is two-fold, modulation of the compressor output and avoidance of collision with the cylinder head. For the purpose of collision avoidance especially, knowledge of the absolute position is critical, which makes the majority of existing methods presented unsuitable.

In this work a series of nonlinear observers are utilized to obtain observations for signals in the mechanical dynamics. Each of these observers includes a robust integral of sign of error (RISE) term to compensate for uncertainties in the system dynamics. The first observer uses a motor current measurement along with knowledge of the motor voltage and the system's electrical model to arrive at an observed velocity. Unlike other methods, which essentially solve the electrical dynamic equation for velocity, this is

2

a robust feedback based observer. The second observer utilizes a velocity measurement along with knowledge of the system's mechanical model to arrive at an observation for piston acceleration. This observer avoids the need to take noisy numerical derivatives to obtain an acceleration signal such as in [6]. A Lyapunov stability analysis is presented in [17] to prove stability and convergence for these two observers with experimental results providing further validation. By using the observed velocity from the first observer in place of the velocity measurement required by the second observer the two observers are able to run in parallel using only a single current measurement. A gas force observer, derived separately, requires measurement of both position and velocity and so cannot be implemented sensorlessly either alone or in parallel. As such this observer is intended for laboratory use where full state measurements are available and is useful for characterization of the gas force.

The developed velocity and acceleration observers are then utilized to obtain observations of per-cycle system states which are relevant to the system control objectives. The observed velocity signal is used to obtain knowledge of the phase difference between the piston velocity with respect to the motor current. This observed phase difference is used as an indicator of system resonance and is used to achieve the system level control objective of maximum efficiency via a search algorithm based controller.

The observed acceleration signal is used in tandem with the observed velocity and motor current to obtain knowledge of the minimum position of the piston, known as top dead center. Unlike the majority of methods present in the literature this is an absolute position estimation which includes the DC bias induced by the force of gas compression and requires no numerical derivatives. Thus this observed top dead center position can be used to achieve the top dead center control objective and thus prevent collision and modulate compressor output. This controller uses the peak motor current as its control input since this current is proportional to the motor force which actuates the motor. This desired motor current is then used as a reference to a third controller which achieves regulation control of the amplitude of the motor current. Alternatively, a tracking controller is also presented which achieves control of the current waveform via a trajectory whose frequency is set by the resonance controller. By controlling the current over the entire cycle instead of only at its peak this controller offers a more sophisticated and direct control over the piston dynamics at the cost of added complexity.

As the afore-mentioned observers require a priori knowledge of the system model and parameters, this work also includes an investigation of estimation schemes for the parameters of the various dynamics which comprise the linear compressor system model. Least-squares algorithms are commonly used to calculate parameters over a specified interval of samples. In [17] we see how this method can be applied to time-varying parameters in linear systems and [8] shows an implementation specifically for linear compressors.

For this work an adaptive least-squares algorithm as described in [18] was investigated. This algorithm has been shown to be effective in estimation problems for other systems with similar models [19], [20]. Due to the fact that gas force is highly nonlinear and difficult to measure, this method is considered only for the electrical dynamics, requiring measurement of the motor current, voltage, and piston velocity. The need for a velocity measurement makes this method unsuitable for sensorless application, but it may be usable for production testing. It should be noted that due its dependence on parameter values it is not possible to use the velocity observer developed in place of this measurement. Doing so would create a null-space [21] in which a unique solution is unattainable for either problem.

The remainder of this work will proceed as follows: in Section 2 the system model will be presented with its constituent thermodynamic, mechanical, and electrical dynamic equations, in Sections 3 and 4 the simulation and experimental platforms, respectively, which were used in testing of the developed algorithms will be detailed; in Section 5 parameter estimation schemes for the electrical and mechanical parameters of the compressor are developed using the adaptive least-squares algorithm; in Section 6 real-time observers are developed for the piston velocity, acceleration, force of gas compression, position and pressures; in Section 7 we show how the velocity and acceleration observers can be used to obtain observations of relevant per-cycle system states; in Section 8 we show how these per-cycle observations can be utilized to develop regulation controllers which together achieve the joint system level of objectives of stroke control and resonance tracking; in Section 9 a more sophisticated current controller is presented as a possible replacement for the regulation controller put forth in Section 8. Concluding remarks are provided following this section.

2   LINEAR VAPOR COMPRESSOR SYSTEM MODEL

A representation of the construction of a linear compressor is given in Figure 1. As shown, this device consists of a compression chamber whose piston is actuated by a linear motor. This construction creates three levels of coupled dynamics within the system. At the lowest level the oscillation of the piston in the chamber causes compression, decompression, suction, and discharge of the working gas as it cyclically pumps gas from lower to higher pressures. The thermodynamics which dictate this compression cycle cause a resultant force on the piston which couple into its mechanical dynamics. This mechanical dynamic is then cross-coupled with the electrical dynamics of the current induced in the stator coils via the motor force coupled into the mechanical dynamics and the back EMF coupled into the electrical dynamics.
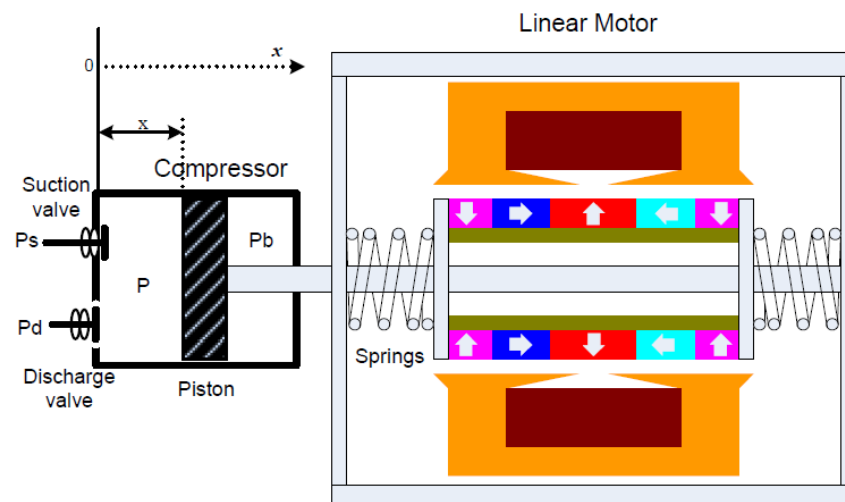
Figure 1. Representation of a typical linear vapor compressor [16].

2.1   THERMODYNAMIC SYSTEM MODEL

The thermodynamics which dictate the chamber pressure $P(t)$ can be represented by the pressure-displacement diagram shown in Figure 2. This diagram shows the chamber pressure as a function of the piston position $x(t)$, as it relates to the discharge and suction pressures, $P_d \in \mathbb{R}$ and $P_s \in \mathbb{R}$, respectively. We can see from this figure that the chamber pressure $P(t)$ is always greater than or equal to the suction pressure P_s.
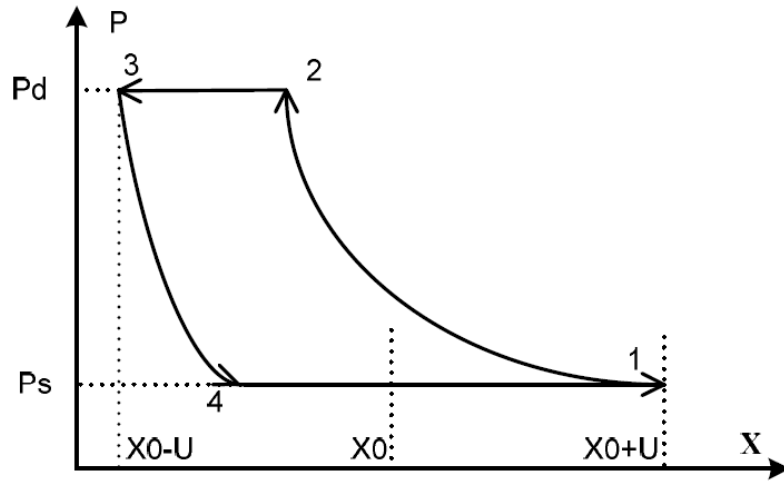
Figure 2. Pressure-displacement curve for a linear vapor compressor [16].

As shown in Figure 2 four different stages make up the compression cycle, resulting in a piecewise continuous chamber pressure $P(t)$. The resultant force imposed on the piston by this gas compression, denoted as $F_g(t) \in \mathbb{R}$, is related to the pressure difference across the piston head as shown in the following equation:

$$F_g \triangleq A_p(P(t) - P_b) \tag{1}$$

where $P(t) \in \mathbb{R}$ is the pressure of the compression chamber, $A_p \in \mathbb{R}$ is the cross-sectional area of the piston, and $P_b \in \mathbb{R}$ is the pressure on the back side of the piston head. In a typical compression cycle, P_b can be assumed to be equal to the suction pressure P_s. From the assumption that $P_b = P_s$, we can see from Fig. 2 and (1) that $F_g \geq 0$ for all t. A detailed description of the piecewise chamber pressure and gas force

through the four stages shown in Figure 2 is given in Table 1 below. Note that the parameter $n \in \mathbb{R}$ denotes the specific heat ratio for the working gas.

Table 1

Pressure and Gas Force Definitions for Isentropic Compression Cycle

Region	Description	$P(t)$	$F_g(t)$
$[1] - [2]$	**Compression Stage** - Suction valve closes at BDC [1] and gas is compressed as piston moves back towards the head. Chamber pressure increases from suction to discharge pressure in an isentropic process.	$P_s \left(\dfrac{X_{BDC}}{x(t)} \right)^n$	$A_p \left(P_s \left(\dfrac{X_{BDC}}{x(t)} \right)^n - P_s \right)$
$[2] - [3]$	**Discharge Stage** - Discharge valve opens when chamber pressure reaches discharge pressure at [2]. Chamber pressure remains constant while valve is open.	P_d	$A_p(P_d - P_s)$
$[3] - [4]$	**Decompression Stage** - Discharge valve closes at TDC [3] and gas is decompressed as piston moves away from the head. Chamber pressure decreases from discharge to suction pressure in an isentropic process.	$P_d \left(\dfrac{X_{TDC}}{x(t)} \right)^n$	$A_p \left(P_d \left(\dfrac{X_{TDC}}{x(t)} \right)^n - P_s \right)$
$[4] - [1]$	**Suction Stage** - Suction valve opens when chamber pressure reaches suction pressure at [4]. Chamber pressure remains constant while valve is open.	P_s	$A_p(P_s - P_s) = 0$

2.2   MECHANICAL SYSTEM MODEL

The mechanical dynamics of this system can be expressed mathematically as follows

$$F_m + F_g = M\ddot{x} + C\dot{x} + K(x - L_0) \tag{2}$$

$$F_m = \alpha I \tag{3}$$

where $F_m(I) \in \mathbb{R}$ is the motor force, $M \in \mathbb{R}$ is the mass of the piston, $C \in \mathbb{R}$ is the coefficient of friction, $K \in \mathbb{R}$ is the combined stiffness of the springs connecting the piston to the chassis, $x(t) \in \mathbb{R}$ is the position of the piston with respect to the cylinder head, $\dot{x}(t), \ddot{x}(t) \in \mathbb{R}$ are respectively the first and second

7

derivatives of $x(t)$, i.e. velocity and acceleration, and $L_0 \in \mathbb{R}$ is the equilibrium position of the piston with respect to the cylinder head. In (3) $\alpha \in \mathbb{R}$ is the motor constant and $I(t) \in \mathbb{R}$ is the motor current.

A set of terms are used within this work to refer to per cycle metrics which describe the stroke of the piston under steady-state conditions. The point during a cycle at which the piston is closest to the cylinder head is referred to as top dead center and is here denoted as $x_{TDC} \in \mathbb{R}$. The point at which the piston is farthest from the cylinder head during a cycle is referred to as bottom dead center and is denoted as $x_{BDC} \in \mathbb{R}$. The distance traveled between these two points is referred to as the stroke length and is denoted as $\Delta x_{SL} \in \mathbb{R}$ which can be defined as

$$\Delta x_{SL} \triangleq x_{BDC} - x_{TDC}. \tag{4}$$

The point halfway between top and bottom dead center is to as the midstroke and is denoted as $x_{mid} \in \mathbb{R}$. Based on the dynamics of (2) and the fact that $F_g(t) \geq 0$ we can see that increasing gas force has the effect of increasing the midstroke of the piston away from x_0.

This system has a frequency at which the mechanical efficiency reaches its maximum, referred to as the resonant frequency. Since the mechanical output power of the linear motor is a product of the motor force and the piston velocity, we can see that this power and therefore the system efficiency is maximized when the force $F_m(t)$ is in phase with the piston velocity $\dot{x}(t)$. From the dynamics in (2) and (3) we can see that this phase difference is a function of the system frequency excited by the current $I(t)$. For a standard mass-spring-damper system the resonant frequency is fixed, however, the addition of the nonlinear gas compression force causes this frequency to change with the thermodynamic load.

2.3   ELECTRICAL SYSTEM MODEL

An equivalent electrical circuit model for the linear motor which drives the compressor piston is shown in Fig. 3. From this circuit model an electrical dynamic equation can be written as

$$v_a = L_i \dot{I} + R_i I + \alpha \dot{x} \tag{5}$$

where $v_a(t) \in \mathbb{R}$ is the voltage applied to the motor, $\dot{I}(t)$ is the derivative of the motor current, $L_i \in \mathbb{R}$ is the inductance of the motor windings, and $R_i \in \mathbb{R}$ is the resistance of the motor windings. This model is a simplification of the machine dynamics in that it assumes that all machine parameters are constant. In

reality the motor constant α and the inductance L_i vary with position $x(t)$ due to the finite length of the stator [16].
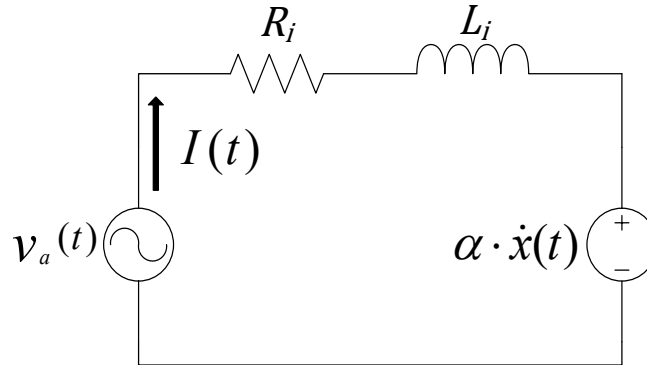
Figure 3. Equivalent electrical circuit model of a linear motor.

2.4 POWER ELECTRONIC SYSTEM MODEL

For this application a voltage source inverter is used to generate the voltage applied to the motor $v_a(t)$. Figure 4 below shows the h-bridge topology used for this system. This generalized topology shows a bulk capacitance supporting a DC bus voltage V_{dc}. The source of this DC bus may be a battery, the output of another converter, or in most cases a rectifier. In this model we assume that the ripple on this DC bus is negligible and thus that V_{dc} can be treated as a constant.
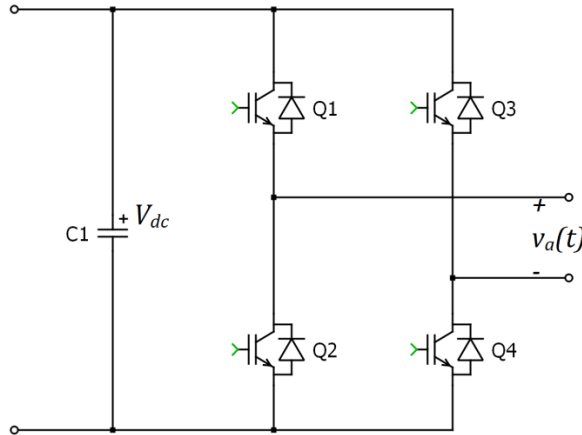
Figure 4. H-bridge inverter topology.

As shown this topology consists of two pairs of series-connected semiconductor switching devices, each comprising what is referred to as a switching leg. The switches in each leg are driven with complementary gate signals with appropriate dead-time to prevent shoot-through events, i.e. a case when both switches are "on" at the same time, which would result in the DC source being short-circuited. Through the management of these gate signals each switching leg is capable of outputting a voltage of $\pm V_{dc}$ at its midpoint. By considering the differential voltage between the two switching leg outputs we can see that the output voltage $v_a(t)$ has three potential voltage states: $-V_{dc}, 0, V_{dc}$. A pulse width modulation scheme can then be used to design a duty cycle for each switching leg which achieves a desired AC reference voltage. A unipolar PWM switching scheme is selected for this application for its superior total harmonic distortion (THD) over other schemes [22].

Provided that the switching frequency f_{sw} of the PWM is sufficiently higher than the frequency of the reference AC voltage which is being generated we find that the frequency spectrum of the inverter output voltage $v_a(t)$ is identical to that of the reference AC voltage with additional sidebands starting at $2f_{sw}$ [22]. Assuming that the inductance of the motor L_i is sufficiently high, we can assume that these high frequency sidebands are effectively filtered and have negligible effect on the system. Thus in our later analysis of the system electrical dynamics we can ignore the high frequency switching effects and consider that the inverter output is equal to the reference voltage, i.e. that the inverter is an ideal AC source. Note that this assumption is valid only if the frequency of $v_a(t)$ is sufficiently smaller than f_{sw}.

3 SIMULATION PLATFORM

The Matlab/Simulink software package was used for simulation of the system model detailed in Section II to be used for validation of the subsequently developed algorithms. The parameters used for this model are given in Table 2 below. These parameters reflect the nominal values of the real compressor utilized in the experimental platform described in the subsequent section. This model includes a C-coded S-function block which is used to model the highly nonlinear piecewise compression cycle thermodynamics. The PLECS Blockset was also used to model the h-bridge inverter detailed in Section 2.4. This model uses a DC bus of $V_{dc} = 350 \, [V]$ and a switching frequency of $f_{sw} = 2 \, [kHz]$. This configuration mirrors the actual inverter utilized in the experimental setup and detailed in the following section. A variable step ode45 solver was utilized for this simulation model.

Table 2

Linear Vapor Compressor Simulation Model Parameters

Parameter	Name	Value	Units
R_i	Stator Winding Resistance	6.3	$[\Omega]$
L_i	Stator Winding Inductance	0.346	$[H]$
α	Motor Constant	75.7	$[N/A]$
M	Piston Mass	0.65	$[kg]$
C	Piston Friction Coefficient	4.5	$[N \cdot s/m]$
K	Spring Constant	66,700	$[N/m]$
P_d	Discharge Pressure	120	$[psi]$
P_s	Suction Pressure	16.6	$[psi]$
A_p	Piston Area	5.3×10^{-4}	$[m^2]$

n	Specific Heat Ratio of Refrigerant	1.07	

The majority of algorithms developed and presented in this work have been tested both in simulation and experimentally. For the sake of brevity, simulation results are only provided in cases where successful experimental results are unavailable.

4   EXPERIMENTAL PLATFORM

4.1   HARDWARE DESIGN

An experimental setup was constructed for real-time implementation of the developed algorithms. A block diagram of this experimental setup is shown in Figure 5. The compressor was setup to compress air with the suction valve open to room air. The discharge valve was connected to a nozzle, to adjust the outlet flow and allow for the buildup of pressure within the system. A pressure gauge was placed in series with the nozzle to measure of the discharge pressure of the compressor. An H-bridge inverter with a 350 [V] DC bus provided by an AC/DC converter and a 2 [kHz] unipolar switching scheme [22] with the same topology shown in Figure 4 was used to generate the motor voltage $v_a(t)$ applied to the linear compressor. A LEM LA25-NP Hall-effect current sensor was used to obtain the current measurement $I(t)$. A U.S. Digital EM1-0-250-I optical encoder with a corresponding LIN-250-1-1 transmissive linear strip was used to measure the displacement $x(t)$. This measurement was used as a reference for testing of sensorless control schemes and also utilized in a number of offline algorithms.
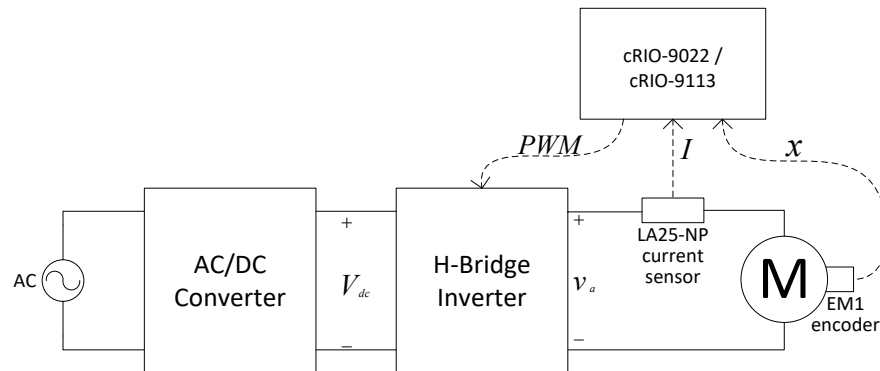
Figure 5. Block diagram of experimental hardware setup.

A National Instruments CompactRIO device consisting of a cRIO-9022 controller and a cRIO-9113 chassis with onboard Virtex-5 LX50 FPGA was selected for execution of the developed algorithms. NI

modules were selected to meet the I/O requirements of the project. An NI-9401 digital output module was used for generation of the PWM signals which control the inverter switching as well as other digital communication. An NI-9411 digital input module was used for reading the digital pulse trains generated by the encoder. Finally, an NI 9215 analog input module was used for measurement of the current sensor voltage output. A numerical derivative was used to obtain a velocity signal $\dot{x}(t)$ from the measured displacement $x(t)$. A 4th order Butterworth filter with cutoff frequency of 200 [Hz] was used to filter the measured current and velocity signals.

4.2   SOFTWARE DESIGN

In order to execute the variety of control, observation, and estimation schemes developed in this work a robust and flexible software setup was developed in the LabVIEW development suite. This setup consists of a hierarchy of three main programs, or virtual instruments (VIs) as they are called in LabVIEW, which each run on a different hardware target. As mentioned in the previous section the CompactRIO consists of two parts, a chassis with onboard FPGA and a controller with a real-time processor. The CompactRIO was setup to run in FPGA mode for maximum performance and functionality, meaning that all I/O are accessed at the FPGA level. For this reason all data acquisition and algorithms are executed on the FPGA in a program which we will refer to as the FPGA VI. This FPGA VI is typically run at a sample and loop rate of 50 [kHz] although faster sample rates were achievable.

Real-time waveform data to be used for visualization is transferred losslessly to the Real-Time VI via DMA (direct memory access) FIFO (first in, first out) data structures. This Real-Time VI runs on the real-time processor of the CompactRIO and its primary function is to control data transfer between the FPGA VI and the Host VI which runs on the host PC. This data transfer includes the waveform data previously mentioned as well as commands from the Host VI to the FPGA VI and indicator data from the FPGA VI to the Host VI. Communication between the Real-Time VI and the Host VI is achieved over a hardwired Ethernet connection.

The primary function of the Host VI is to serve as a user interface (UI) allowing for visualization and recording of the desired waveform data as well as control over all algorithm parameters. The Real-Time VI and Host VI were written in such a way that they are easily interfaced with a variety of versions of the

FPGA VI. In turn all versions of the FPGA VI, even those implementing vastly different algorithms, incorporated the same data transfer code to allow them to be used interchangeably. A representation of the software architecture described is shown in Figure 6 below.
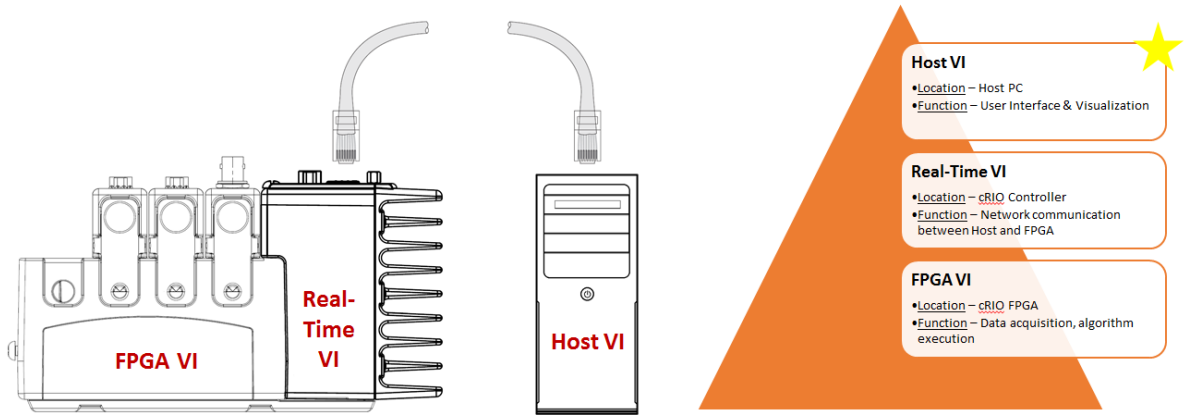
Figure 6. Diagram of software architecture and hardware integration for NI CompactRIO platform.

5   PARAMETER ESTIMATION

5.1   ELECTRICAL PARAMETERS

5.1.1   ESTIMATOR DESIGN

An adaptive least-squares estimator is to be developed for estimation of the electrical parameters of the linear motor model presented in Section 2.3 based on the dynamics in (5). For the proceeding mathematical analysis the following assumptions are made.

Assumption 1: The parameters R_i, α and L_i are unknown with R_i being a constant and α and L_i being slowly time-varying such that $\dot{\alpha}(t) \approx 0$ and $\dot{L}_i(t) \approx 0$.

Assumption 2: The variables $v_a(t), I(t), \dot{I}(t), x(t), \dot{x}(t)$ are all piecewise continuous and bounded and, with the exception of $\dot{I}(t)$, all are measurable.

Assumption 3: The initial conditions of the variables $v_a(t_0), I(t_0), \dot{I}(t_0), \dot{x}(t_0)$ are all equal to zero; i.e. estimation begins when the machine is at rest and unexcited.

An adaptive least-squares estimator for the unknown electrical parameters, α, R_i, and L_i is to be designed utilizing the electrical dynamic equation (5). To facilitate the estimator development this equation is rewritten as a linear combination of constants and variables as follows:

$$\Phi \triangleq W\theta_e \tag{6}$$

where $\Phi(t) \in \mathbb{R}, W(t) \in \mathbb{R}^{1\times 3}$ are defined as follows

$$\Phi \triangleq \begin{bmatrix} \dot{I} \end{bmatrix} \tag{7}$$

$$W \triangleq \begin{bmatrix} v_a & -I & -\dot{x} \end{bmatrix} \tag{8}$$

and $\theta_e \in \mathbb{R}^3$ represents the unknown parameters to be estimated

$$\theta_e \triangleq \begin{bmatrix} \dfrac{1}{L_i} & \dfrac{R_i}{L_i} & \dfrac{\alpha}{L_i} \end{bmatrix}^T. \tag{9}$$

To implement the estimator design it is required that all signals in (6) be measureable, but this is not the case for $\Phi(t)$ due to its dependence on $\dot{I}(t)$. A filtering technique is utilized to overcome this dependence. The plant of estimation to be used is a linearly stable, strictly proper low-pass filter $H_e(s) \in \mathbb{C}$ defined in the Laplace domain as

$$H_e(s) \triangleq \frac{b_e}{s + b_e} \tag{10}$$

where $b_e \in \mathbb{R}^+$ is a constant gain and $s \in \mathbb{C}$ is the Laplace variable. This value determines the cutoff frequency of the filter and should be selected in consideration of noise cancellation versus signal attenuation. Convolving this filter with the signal $\Phi(t)$ a filtered plant output $\Phi_f(t) \in \mathbb{R}$ can be defined as follows

$$\Phi_f(t) \triangleq h_e(t) * \Phi(t) \tag{11}$$

where $h_e(t) \in \mathbb{R}$ is the inverse Laplace transform of $H_e(s)$. Substituting (6) into (11) a form of the filtered signal $\Phi_f(t)$ can be written as follows

$$\Phi_f(t) \triangleq W_f(t)\theta_e \tag{12}$$

where $W_f(t) \in \mathbb{R}^{1 \times 3}$ is defined as

$$W_f(t) \triangleq h_e(t) * W(t). \tag{13}$$

The dependence of $\Phi_f(t)$ on $\dot{I}(t)$ can then be eliminated by utilizing the differentiation property of Laplace transforms as shown below

$$\dot{I}(s) = sI(s) - i(t_0) \tag{14}$$

where $I(s) \in \mathbb{C}$ is the Laplace transform of $I(t)$. Given from Assumption 3 that $i(t_0) = 0$, this term can be eliminated from (14). From this a modified filter $H_e'(s) \in \mathbb{C}$ can be defined as

$$H_e'(s) \triangleq \frac{b_e s}{s + b_e} \tag{15}$$

Utilizing this modified filter, $\Phi_f(t)$ can be rewritten in terms of the measurable signal $I(t)$ as follows

$$\Phi_f(t) = h_e'(t) * I(t) \tag{16}$$

where $h'_e(t) \in \mathbb{R}$ is the inverse Laplace transform of $H'_e(s)$. The object of the estimator is to update values of the estimate vector $\hat{\theta}_e$ according to the error of the estimates. Estimate error is defined as follows

$$\tilde{\theta}_e \triangleq \theta_e - \hat{\theta}_e. \tag{17}$$

Due to the fact that θ_e is unknown, the error signal $\tilde{\theta}_e$ cannot be directly calculated. However, an alternate error signal, $\tilde{\Phi}_f(t)$, can be generated by first substituting the estimate vector $\hat{\theta}_e$ into (12) to obtain an estimate of the plant input $\hat{\Phi}_f(t)$ as shown

$$\hat{\Phi}_f \triangleq W_f \hat{\theta}_e \tag{18}$$

$$\tilde{\Phi}_f \triangleq \Phi_f - \hat{\Phi}_f. \tag{19}$$

By substituting (12) and (18) into (19) and utilizing (17) it can be seen that this error signal is related to the actual estimate error as follows

$$\tilde{\Phi}_f = W_f \tilde{\theta}_e. \tag{20}$$

From the error signal $\tilde{\Phi}_f(t)$ an adaptive update rule using the least-squares estimation method can be developed as follows

$$\dot{\hat{\theta}}_e \triangleq -k_e \frac{P_e W_f^T \tilde{\Phi}_f}{1 + \gamma_e W_f P_e W_f^T} \tag{21}$$

where k_e, $\gamma_e \in \mathbb{R}^+$ are constant gains and $P_e(t) \in \mathbb{R}^{3\times3}$ is the covariance matrix defined by the update equation

$$\dot{P}_e \triangleq -k_e \frac{P_e W_f^T W_f P_e}{1 + \gamma_e W_f P_e W_f^T} \tag{22}$$

where $P_e(t_0) = \rho_e I_3$, $\rho_e \in \mathbb{R}^+$ is a constant gain, and $I_3 \in \mathbb{R}^{3\times3}$ is the standard identity matrix. These gain values k_e, γ_e and ρ_e directly affect the convergence rate of the system as well as its sensitivity to noise. The value of $\hat{\theta}_e$ resulting from the update law in (21) can be used to infer estimates of the unknown parameters α, R_i, and L_i by means of the following set of equations

$$\hat{\alpha} = \frac{\hat{\theta}_{e_3}}{\hat{\theta}_{e_1}}, \qquad \hat{R}_i = \frac{\hat{\theta}_{e_2}}{\hat{\theta}_{e_1}}, \qquad \hat{L}_i = \frac{1}{\hat{\theta}_{e_1}} \tag{23}$$

Remark 5.1.1: From (23) *it is clear that special care needs to be taken to avoid* $\hat{\theta}_{e_1}(t) = 0$. *To achieve this condition, the projection algorithm described in Section 2.3.1 of* [18] *must be utilized. This algorithm takes into account* $\hat{\theta}_{e_1}(t)$ *and* $\dot{\hat{\theta}}_{e_1}(t)$ *to keep* $\hat{\theta}_{e_1}(t) > 0$, *while maintaining stability and convergence of the least-squares estimation strategy.*

Theorem 5.1.1: The least-squares algorithm described by (21) and (22) ensures that $\tilde{\theta}_e(t) \to 0$ as $t \to \infty$ provided the following sufficient conditions are met: (i) the plant of estimation is strictly proper, (ii) the

input is piecewise continuous and bounded, (iii) the output of the plant of estimation is bounded, and (iv) the following persistence of excitation condition holds

$$\beta_1 I_3 \leq \int_{t_0}^{t+\delta} W_f^T(\tau) W_f(\tau) d\tau \leq \beta_2 I_3 \tag{24}$$

where $\beta_1, \beta_2, \delta \in \mathbb{R}^+$ are constants and $I_3 \in \mathbb{R}^{3 \times 3}$ is the standard identity matrix.

Proof: To prove that $\tilde{\theta}_e(t) \to 0$ as $t \to \infty$, Theorem 2.5.3 from [18] is followed directly. Condition (i) is proved to be valid as the plant of estimation described in (10) can be seen to be strictly proper. Condition (ii) is met by recognizing that the reference input to the plant $\Phi(t)$ is solely dependent upon the signal $\dot{I}(t)$ which as stated in Assumption 2 is bounded and piecewise continuous. To prove condition (iii) is met: by utilizing standard linear analysis tools it can be shown that since $\Phi(t)$ is bounded $\Phi_f(t), \dot{\Phi}_f(t) \in \mathcal{L}_\infty$. Condition (iv) is dependent on the way in which the system is excited. As such, it will be shown in the implementation of this algorithm in Section 5.1.2 that the operating conditions used satisfy this condition.

5.1.2   EXPERIMENTAL RESULTS

The parameter estimator described in (21) and (22) was implemented on the experimental platform under the conditions stated. The resulting gas force is highly nonlinear and imparts significant harmonic content into the mechanical dynamics. This harmonic content is propagated into the electrical dynamic equation via the velocity in the back EMF term (5), thus fulfilling the persistence of excitation mentioned in Theorem 5.1.1. Gain values of $b_e = 100, k_e = 40$, and $\rho_e = 0.2$ were selected via trial and error for optimal convergence and noise sensitivity.
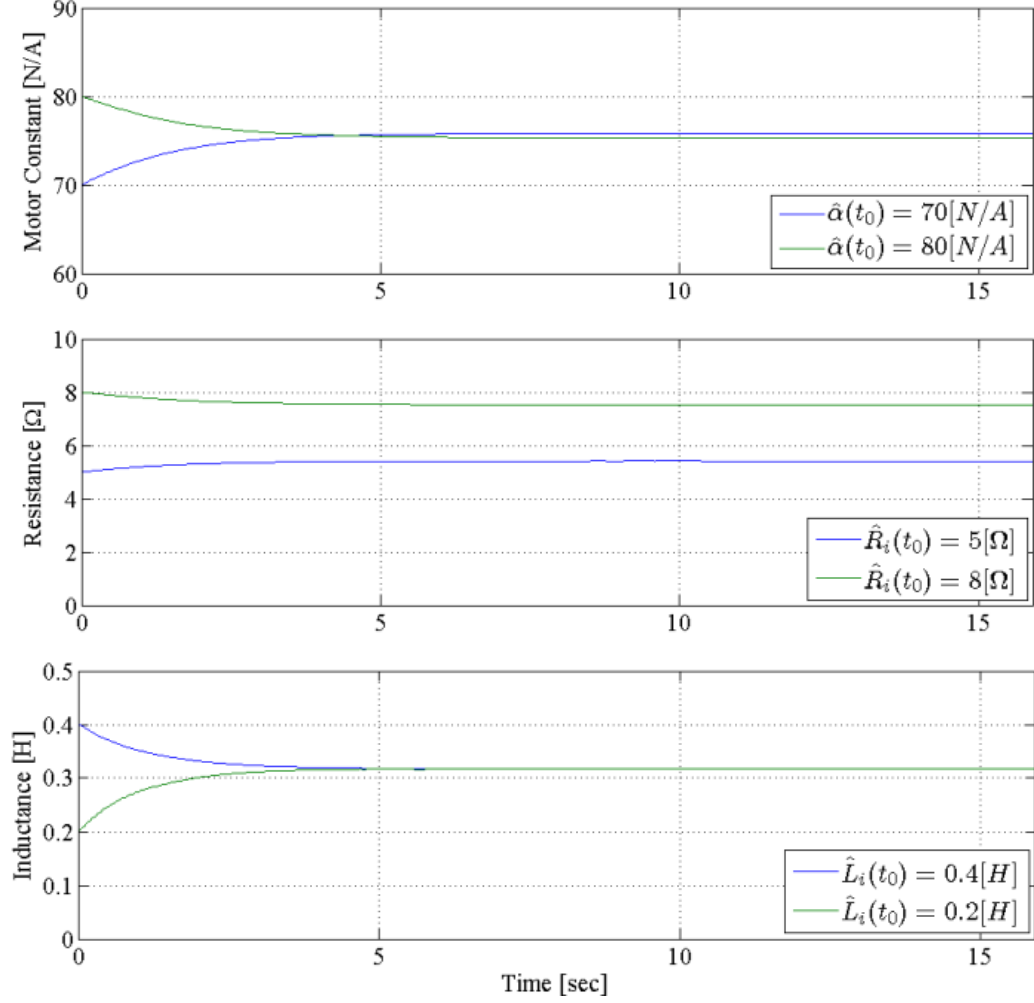
Figure 7. Estimation results for the electrical parameters α, R_i, L_i.

Two different trials were performed using different sets of initial conditions. The first trial used values of $\hat{\alpha}(t_0) = 70\ [N/A], \hat{R}_i(t_0) = 5\ [\Omega]$ and $\hat{L}_i(t_0) = 0.4\ [H]$, while the second used values of $\hat{\alpha}(t_0) = 80\ [N/A], \hat{R}_i(t_0) = 8\ [\Omega]$ and $\hat{L}_i(t_0) = 0.2\ [H]$. The results of this experiment are shown in Figure 7. From this we see little to no dependence on initial values for the estimates of α and L_i, while a stronger dependence is seen for R_i. Using the average of the convergence values for each trial, the following parameter estimates were identified for use in the observer algorithms: $\hat{\alpha} = 75.6\ [N/A], \hat{R}_i = 6.47\ [\Omega], \hat{L}_i = 0.318\ [H]$. A DC resistance test provides further confidence for the resistance estimate with a result of $6.5\ [\Omega]$.

We can make sense of the differences in convergence of the three parameters by considering the relative magnitudes of the parameter/signal pairs in (6). From (23) we can see that the convergence of $\hat{R}_i$ is exclusively dependent on $\hat{\theta}_{e_2}$ which corresponds to the regressor term W_2 from (8). Using the rms values mentioned previously and the average converged estimator values, an rms of the parameter/signal pair $W_2\hat{\theta}_{e_2}$ can be estimated as 10.13 [A/s] while the rms of $W_1\hat{\theta}_{e_1}$ and $W_3\hat{\theta}_{e_3}$ are 417.92 [A/s] and 385.13 [A/s], respectively. The difference in the relative magnitude of the term $W_2\hat{\theta}_{e_2}$ compared to the other terms in (6) for this excitation explains why weaker convergence is seen for $\hat{\theta}_{e_2}$ and therefore $\hat{R}_i$ [18]. Selection of a more balanced excitation could alleviate this problem, but such an excitation would be of no practical interest to this application, and since a DC resistance test is easily obtainable there is no motivation to do so.

5.2   MECHANICAL PARAMETERS

5.2.1   ESTIMATOR DESIGN

The proceeding mathematical analysis requires an additional assumption to be added to those presented in Section 5.1.1.

Assumption 4: The machine is operating under such conditions that the gas force F_g is constant and equal to zero.

Estimation of the unknown mechanical parameters, M, C, and K utilizing an adaptive least-squares algorithm is performed utilizing the mechanical dynamic equations (2) and (3). Coupling these two equations and simplifying them via Assumption 5 the following form of the mechanical dynamics can be written

$$\Psi \triangleq Y\theta_m \tag{25}$$

where $\Psi(t) \in \mathbb{R}$, $Y(t) \in \mathbb{R}^{1\times3}$ are defined as follows

$$\Psi \triangleq [\ddot{x}] \tag{26}$$

$$Y \triangleq [-\dot{x} \quad -(x - L_0) \quad I] \tag{27}$$

and $\theta_m \in \mathbb{R}^3$ represents the unknown parameters to be estimated

$$\theta_e \triangleq \begin{bmatrix} \dfrac{C}{M} & \dfrac{K}{M} & \dfrac{\alpha}{M} \end{bmatrix}^T. \tag{28}$$

To implement the estimator design it is required that all signals in (25) be measureable, but this is not the case for $\Psi(t)$ due to its dependence on $\ddot{x}(t)$. A filtering technique is utilized to overcome this dependence. The plant of estimation to be used is a linearly stable, strictly proper low-pass filter $H_m(s) \in \mathbb{C}$ defined in the Laplace domain as

$$H_m(s) \triangleq \frac{b_m}{s + b_m} \tag{29}$$

where $b_m \in \mathbb{R}^+$ is a constant gain. This value determines the cutoff frequency of the filter and should be selected in consideration of noise cancelation versus signal attenuation. Convolving this filter with the signal $\Psi(t)$ a filtered plant output $\Psi_f(t) \in \mathbb{R}$ can be defined as follows

$$\Psi_f(t) \triangleq h_m(t) * \Psi(t) \tag{30}$$

where $h_m(t) \in \mathbb{R}$ is the inverse Laplace transform of $H_m(s)$. Substituting (25) into (30) a form of the filtered signal $\Psi_f(t)$ can be written as follows

$$\Psi_f(t) \triangleq Y_f(t)\theta_m \tag{31}$$

where $Y_f(t) \in \mathbb{R}^{1 \times 3}$ is defined as

$$Y_f(t) \triangleq h_m(t) * Y(t). \tag{32}$$

The dependence of $\Psi_f(t)$ on $\ddot{x}(t)$ can then be eliminated by utilizing the differentiation property of Laplace transforms as shown below

$$\ddot{X}(s) = s\dot{X}(s) - \dot{x}(t_0) \tag{33}$$

where $\dot{X}(s) \in \mathbb{C}$ is the Laplace transform of $\dot{x}(t)$. Given from Assumption 3 that $\dot{x}(t_0) = 0$, this term can be eliminated from (33). From this a modified filter $H_m{}'(s) \in \mathbb{C}$ can be defined as

$$H_m'(s) \triangleq \frac{b_m s}{s + b_m} \tag{34}$$

Utilizing this modified filter, $\Psi_f(t)$ can be rewritten in terms of the measurable signal $\dot{x}(t)$ as follows

$$\Psi_f(t) = h_m'(t) * \dot{x}(t) \tag{35}$$

where $h'_m(t) \in \mathbb{R}$ is the inverse Laplace transform of $H'_m(s)$. The object of the estimator is to update values of the estimate vector $\hat{\theta}_m$ according to the error of the estimates. Estimate error is defined as follows

$$\tilde{\theta}_m \triangleq \theta_m - \hat{\theta}_m. \tag{36}$$

Due to the fact that θ_m is unknown, the error signal $\tilde{\theta}_m$ cannot be directly calculated. However, an alternate error signal, $\tilde{\Psi}_f(t)$, can be generated by first substituting the estimate vector $\hat{\theta}_m$ into (31) to obtain an estimate of the plant input $\hat{\Psi}_f(t)$ and a corresponding error signal as shown

$$\hat{\Psi}_f \triangleq Y_f \hat{\theta}_m \tag{37}$$

$$\tilde{\Psi}_f \triangleq \Psi_f - \hat{\Psi}_f. \tag{38}$$

By substituting (31) and (37) into (38) and utilizing (36) it can be seen that this error signal is related to the actual estimate error as follows

$$\tilde{\Psi}_f = Y_f \tilde{\theta}_m. \tag{39}$$

From the error signal $\tilde{\Psi}_f(t)$ an adaptive update rule using the least-squares estimation method can be developed as follows

$$\dot{\hat{\theta}}_m \triangleq -k_m \frac{P_m Y_f^T \tilde{\Psi}_f}{1 + \gamma_m Y_f P_m Y_f^T} \tag{40}$$

where k_m, $\gamma_m \in \mathbb{R}^+$ are constant gains and $P_m(t) \in \mathbb{R}^{3 \times 3}$ is the covariance matrix defined by the update equation

$$\dot{P}_m \triangleq -k_m \frac{P_m Y_f^T Y_f P_m}{1 + \gamma_m Y_f P_m Y_f^T} \tag{41}$$

where $P_m(t_0) = \rho_m I_3$, $\rho_m \in \mathbb{R}^+$ is a constant gain. These gain values k_m, γ_m and ρ_m directly affect the convergence rate of the system as well as its sensitivity to noise. The value of $\hat{\theta}_m$ resulting from the update law in (40) can be used to infer estimates of the unknown parameters M, C, and K by means of the following set of equations

$$\hat{M} = \frac{1}{\hat{\theta}_{m_3}} \alpha, \qquad \hat{R}_i = \frac{\hat{\theta}_{m_1}}{\hat{\theta}_{m_3}} \alpha, \qquad \hat{L}_i = \frac{\hat{\theta}_{m_2}}{\hat{\theta}_{m_3}} \alpha \tag{42}$$

Note that the estimates above require knowledge of the motor constant α. This knowledge can be obtained from the estimate $\hat{\alpha}$ in (23), assuming that the electrical parameter estimator has been run previously.

Remark 5.2.1: From (42) *it is clear that special care needs to be taken to avoid* $\hat{\theta}_{m_3}(t) = 0$. *To achieve this condition, the projection algorithm described in Section 2.3.1 of* [18] *must be utilized. This algorithm takes into account* $\hat{\theta}_{m_3}(t)$ *and* $\dot{\hat{\theta}}_{m_3}(t)$ *to keep* $\hat{\theta}_{m_3}(t) > 0$, *while maintaining stability and convergence of the least-squares estimation strategy.*

Theorem 5.2.1: The least-squares algorithm described by (40) and (41) ensures that $\tilde{\theta}_m(t) \to 0$ as $t \to \infty$ provided the following sufficient conditions are met: (i) the plant of estimation is strictly proper, (ii) the input is piecewise continuous and bounded, (iii) the output of the plant of estimation is bounded, and (iv) the following persistence of excitation condition holds

$$\varepsilon_1 I_3 \leq \int_{t_0}^{t+\sigma} Y_f^T(\tau) Y_f(\tau) d\tau \leq \varepsilon_2 I_3 \tag{43}$$

where $\varepsilon_1, \varepsilon_2, \sigma \in \mathbb{R}^+$ are constants and $I_3 \in \mathbb{R}^{3\times3}$ is the standard identity matrix.

Proof: To prove that $\tilde{\theta}_m(t) \to 0$ as $t \to \infty$, Theorem 2.5.3 from [18] is followed directly. Condition (i) is proved to be valid as the plant of estimation described in (29) can be seen to be strictly proper. Condition (ii) is met by recognizing that the reference input to the plant $\Psi(t)$ is solely dependent upon the signal $\ddot{x}(t)$ which as stated in Assumption 2 is bounded and piecewise continuous. To prove condition (iii) is met: by utilizing standard linear analysis tools it can be shown that since $\Psi(t)$ is bounded $\Psi_f(t), \dot{\Psi}_f(t) \in \mathcal{L}_\infty$. Condition (iv) is dependent on the way in which the system is excited. As such, it will be shown in the implementation of this algorithm in Section 5.2.2 that the operating conditions used satisfy this condition.

5.2.2   SIMULATION RESULTS

The simulation model presented in Section 3 was used to validate the adaptive least-squares algorithm for the mechanical parameters of the linear compressor. The plant model was modified such that the force of gas compression was equal to zero per Assumption 4.

Because of the lack of gas force in this simulation a different method was required to fulfill the persistence of excitation mentioned in Theorem 5.2.1. A dual frequency voltage excitation was selected for this purpose with frequencies of 21 and 49 [Hz] utilized and a peak voltage of 40 [V] for each. Gain values of $b_m = 10, k_m = 50$, and $\rho_m = 50$ were selected via trial and error for optimal convergence and noise sensitivity. Initial values of $\hat{\theta}_m(t_0) = [10 \quad 1e5 \quad 100]^T$ were used for the estimator. Estimates for the parameters M, C, and K were calculated according to (42) using the value of α given in Table 2. Fig. 8 shows the results of the simulation and the convergence of all three parameters to the known values used in the plant model.
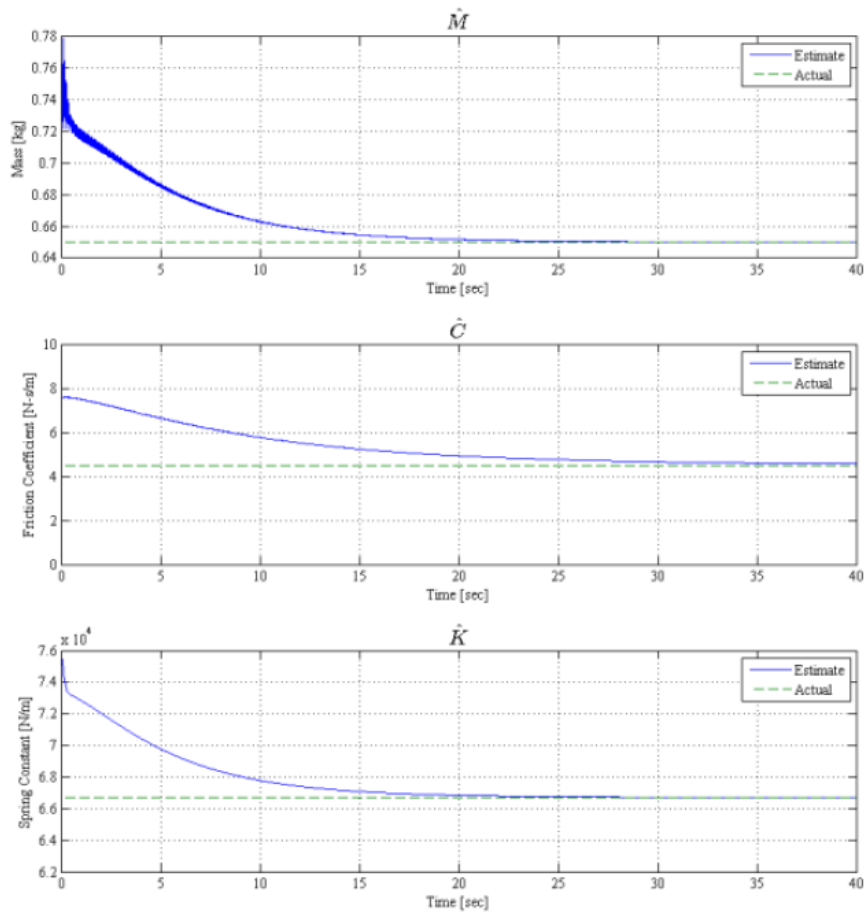
Figure 8. Simulation results for adaptive least-squares mechanical parameter estimation scheme.

25

6   REAL-TIME OBSERVERS

6.1   VELOCITY OBSERVER

The goal of this observer is to accurately observe the piston velocity using only the measured motor current and knowledge of the applied voltage as well as parameter knowledge. From this information a model-based observer is developed for the piston velocity. Development in the subsequent sections will show how this observation can be used to obtain valuable operational information such as system resonance, and ultimately piston position.

6.1.1   OBSERVER DEVELOPMENT

A nonlinear observer is developed for the piston velocity. To facilitate the development of the velocity observer, the electrical dynamics in (5) can be rewritten as

$$\dot{I} = \frac{1}{L_i} v_a - \frac{R_i}{L_i} I - f_V \tag{44}$$

where $f_V(t) \in \mathbb{R}$ is a scaled velocity signal and is defined as follows:

$$f_V \triangleq \frac{\alpha}{L_i} \dot{x}. \tag{45}$$

The proceeding mathematical analysis necessitates a new set of assumptions (previous assumptions are ignored).

Assumption 1: The signals $v_a(t)$ and $I(t)$ are measurable.

Assumption 2: The variables $v_a(t), I(t), \dot{I}(t), x(t), \dot{x}(t), \dot{f}_V(t), \ddot{f}_V(t)$ are all piecewise continuous and bounded, hence there exist positive bounding constants $\zeta_{1_V}, \zeta_{2_V} \in \mathbb{R}^+$ such that $\left| \dot{f}_V(t) \right| < \zeta_{1_V}, \left| \ddot{f}_V(t) \right| < \zeta_{2_V}$

Assumption 3: The machine parameters L_i, R_i, and α are known *a priori* and are constants with respect to time.

The nonlinear observer to be designed for the signal $f_V(t)$ is denoted as $\hat{f}_V(t) \in \mathbb{R}$. For a given $\hat{f}_V(t)$, (44) can be utilized to obtain an observation for $\dot{I}(t)$ defined as

$$\dot{\hat{I}} \triangleq \frac{1}{L_i}v_a - \frac{R_i}{L_i}I - \hat{f}_V. \tag{46}$$

Taking the integral of (46) gives the following observation for $\hat{I}(t)$:

$$\hat{I} = \int_{t_0}^{t}\left(\frac{1}{L_i}v_a(\sigma) - \frac{R_i}{L_i}I(\sigma)\right)d\sigma - \int_{t_0}^{t}\hat{f}_V(\sigma)d\sigma + \hat{I}(t_0). \tag{47}$$

Utilizing (46), (47) and the observation $\hat{f}_V(t)$ the following error signals can be defined for the observer:

$$\tilde{f}_V \triangleq f_V - \hat{f}_V \tag{48}$$

$$e_V \triangleq \hat{I} - I \tag{49}$$

$$\dot{e}_V = \dot{\hat{I}} - \dot{I}. \tag{50}$$

Substituting (44) and (46) into (50) and utilizing (48) gives the following relationship between $\dot{e}_V(t)$ and $\tilde{f}_V(t)$:

$$\dot{e}_V = \tilde{f}_V. \tag{51}$$

A filtered error signal $s_V(t)$ is defined as

$$s_V \triangleq \dot{e}_V + e_V. \tag{52}$$

From the subsequent stability analysis the following observer is designed for the scaled velocity:

$$\dot{\hat{f}}_V \triangleq (k_{1_V} + 1)s_V + k_{2_V}sgn(e_V) \tag{53}$$

where $k_{1_V}, k_{2_V} \in \mathbb{R}^+$ are constant gains and $sgn(\cdot)$ is the signum function. The dependence of (53) on $s_V(t)$ makes it unrealizable per Assumption 4. A realizable from of $\hat{f}_V(t)$ can be obtained by substituting (52) into (53) and integrating both sides of the resulting equation to obtain the following:

$$\hat{f}_V = (k_{1_V} + 1)\left[e_V(t) - e_V(t_0) + \int_{t_0}^{t}e_V(\sigma)d\sigma\right] + k_{2_V}\int_{t_0}^{t}sgn(e_V(\sigma))d\sigma + \hat{f}_V(t_0). \tag{54}$$

Remark 6.1.1: The observer presented in this section may be of particular interest for production-level applications as it does not require measurement of any of the mechanical states of the compressor.

Remark 6.1.2: The stability analysis presented in the appendix proves that the nonlinear observer $\hat{f}_V(t)$ defined in (54) converges to the observed signal $f_V(t)$. Utilizing (45), a velocity observer $\hat{\tilde{x}}_V(t)$ can be written as

$$\hat{x}_V \triangleq \frac{L_i}{\alpha} \hat{f}_V. \tag{55}$$

It is clear from (55) that the accuracy of this observer is directly dependent on the accuracy of the parameters used.

6.1.2   STABILITY ANALYSIS

Theorem 6.1.1: The scaled velocity observer given in (54) ensures that

$$\hat{f}_V(t) \to f_V(t) \quad as \quad t \to \infty \tag{56}$$

provided that the observer gain k_{2_V} is selected to meet the following sufficient condition:

$$k_{2_V} > \zeta_{1_V} + \zeta_{2_V}. \tag{57}$$

Proof: See Appendix.

6.1.3   EXPERIMENTAL RESULTS

The observer described in (54) was implemented on the experimental platform using a current measurement and knowledge of the applied voltage. Model parameters for the observer were selected based on the average results of the electrical parameter estimation detailed in Section 5.1.2. A value of $k_{2_V} = 1.5\times10^5$ was selected to fulfill the gain condition given in (57) based on the expected range of operating conditions. A gain of $k_{1_V} = 4\times10^4$, which acts similarly to a proportional-integral gain, was selected via trial and error for optimal convergence and noise sensitivity. Similar performance was seen for values of $k_{2_V} > 1\times10^5$ and $k_{1_V} > 2\times10^4$ with upper limits for these gains determined by the variable limits of the real-time processor to avoid overflow. At $t = 0$ the observer was initialized.

The results of this experiment are shown in Fig. 9 and 10. Fig. 9 shows the observer error $e_V(t)$ defined in (49) as it converges to approximately zero. Fig. 10 shows the observed velocity $\hat{x}_V(t)$ derived via (55) in comparison with the velocity signal $\dot{x}(t)$ obtained from the encoder measurement. Once the

observer has converged, the ratio of the rms of the error between the observed and actual velocities, taken as a percent of the rms of the actual velocity, is calculated as 2.39%. We can see from Fig. 9 and 10 that the velocity observer is converging much faster than the current observer. From (51) this gives an indication that $\dot{e}_V(t)$ is converging much faster than $e_V(t)$.
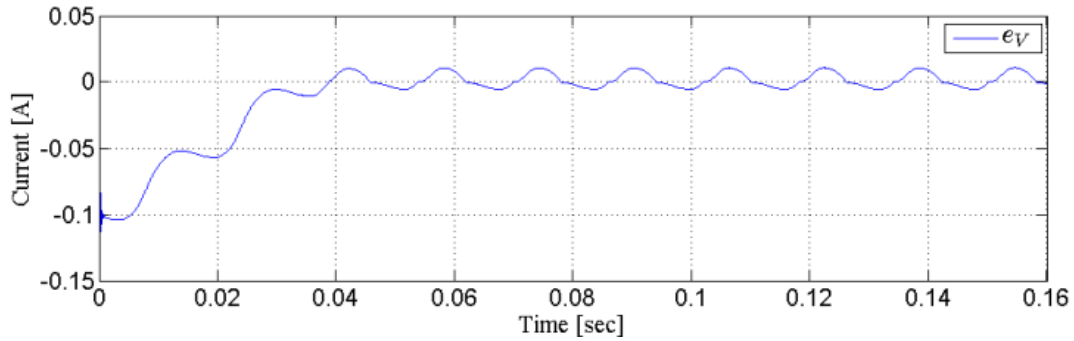
Figure 9. Convergence of observer error $e_V(t)$.
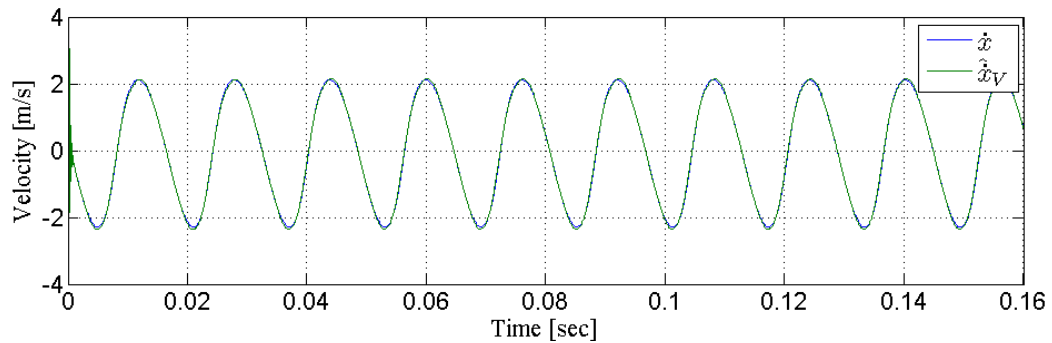
Figure 10. Comparison of velocity, measured $\dot{x}(t)$ and observed $\hat{\dot{x}}_V(t)$.

6.2   ACCELERATION OBSERVER

Our objective is to develop an observer for piston acceleration using measurements for piston velocity, motor current, and parameter knowledge. This observer removes the need for numerical derivatives which unavoidably amplify the measured noise. Due to its reliance on mechanical measurements this observer is not suitable for production purposes, however the following subsection will show how this observer can be modified to remove the need for a piston velocity measurement. Subsequent sections will also show how the resulting acceleration signal can be used to obtain knowledge of the absolute piston position.

6.2.1   OBSERVER DEVELOPMENT

A nonlinear observer is to be developed to observe piston acceleration while accounting for uncertainties in the mechanical dynamics. To facilitate the development of the acceleration observer, the mechanical dynamics described in (2) and (3) can be combined and rewritten as

$$\ddot{x} = \frac{\alpha}{M} I + f_U \tag{58}$$

where $f_U(t) \in \mathbb{R}$ represents the lumped uncertain terms and is defined as follows:

$$f_U \triangleq -\frac{C}{M}\dot{x} - \frac{K}{M}x + \frac{1}{M}F_g. \tag{59}$$

The proceeding mathematical analysis necessitates a new set of assumptions (previous assumptions are ignored).

Assumption 1: The signals $I(t)$ and $\dot{x}(t)$ are measurable.

Assumption 2: The variables $I(t), x(t), \dot{x}(t), \ddot{x}(t), \dddot{x}(t), f_U(t), \dot{f}_U(t), \ddot{f}_U(t)$ are all piecewise continuous and bounded, hence there exist positive bounding constants $\zeta_{1_U}, \zeta_{2_U} \in \mathbb{R}^+$ such that $\left| \dot{f}_U(t) \right| < \zeta_{1_U}, \left| \ddot{f}_U(t) \right| < \zeta_{2_U}$.

Assumption 3: The machine parameters M and α are known *a priori* and are constants with respect to time.

The nonlinear observer to be designed for the uncertain terms comprising $f_U(t)$ is denoted as $\hat{f}_U(t) \in \mathbb{R}$ where the observer is to ensure that $\hat{f}_U(t) \rightarrow f_U(t)$ as $t \rightarrow \infty$. Utilizing $\hat{f}_U(t)$ with (58), an observed acceleration can be defined as

$$\hat{\ddot{x}}_U \triangleq \frac{\alpha}{M} I + \hat{f}_U. \tag{60}$$

Taking the integral of (60) gives the following observation for velocity:

$$\hat{\dot{x}}_U = \int_{t_0}^{t} \frac{\alpha}{M} I(\sigma)\, d\sigma + \int_{t_0}^{t} \hat{f}_U(\sigma) d\sigma \tag{61}$$

Utilizing (60), (61) and the observation $\hat{f}_U(t)$ the following error signals can be defined for the observer:

$$\tilde{f}_U \triangleq f_U - \hat{f}_U \tag{62}$$

$$e_U \triangleq \dot{x} - \hat{\dot{x}}_U \tag{63}$$

$$\dot{e}_U = \ddot{x} - \dot{\hat{x}}_U \tag{64}$$

Substituting (58) and (60) into (64) and utilizing (62) gives the following relationship between $\dot{e}_U(t)$ and $\tilde{f}_U(t)$:

$$\dot{e}_U = \tilde{f}_U. \tag{65}$$

A filtered error signal $s_U(t)$ is defined as

$$s_U \triangleq \dot{e}_U + e_U. \tag{66}$$

From the subsequent stability analysis the following observer is designed for the uncertainty signal:

$$\dot{\hat{f}}_U \triangleq \left(k_{1_U} + 1\right)s_U + k_{2_U}sgn(e_U) \tag{67}$$

where $k_{1_U}, k_{2_U} \in R^+$ are constant gains. The dependence of (67) on $s_U(t)$ makes it unrealizable per Assumption 7. A realizable from of $\hat{f}_U(t)$ can be obtained by substituting (45) into (46) and integrating both sides of the resulting equation to obtain the following:

$$\hat{f}_U = \left(k_{1_U} + 1\right)\left[e_U(t) - e_U(t_0) + \int_{t_0}^{t} e_U(\sigma)d\sigma\right] + k_{2_U}\int_{t_0}^{t} sgn(e_U(\sigma))d\sigma + \hat{f}_U(t_0). \tag{68}$$

Remark 6.2.1: *This observer may be of interest for production-level applications as it does not require measurement of any of the mechanical states of the compressor provided that a velocity observer such as the one described in Section 4 is used in place of the measured velocity.*

Remark 6.2.2: *The stability analysis presented in the appendix proves that the nonlinear observer $\hat{f}_U(t)$ defined in (47) converges to the uncertainty signal $f_U(t)$.*

6.2.2   STABILITY ANALYSIS

Theorem 6.2.1: The observer defined in (68) ensures that

$$\hat{f}_U(t) \rightarrow f_U(t) \quad as \quad t \rightarrow \infty \tag{69}$$

provided that the observer gain k_{2_U} is selected to meet the following sufficient condition:

$$k_{2_U} > \zeta_{1_U} + \zeta_{2_U}. \tag{70}$$

Proof: See Appendix.

6.2.3 EXPERIMENTAL RESULTS

The uncertainty observer described in (68) was implemented on the experimental platform using the filtered current and velocity measurements described previously. Additionally, a numerical derivative was used to obtain an acceleration signal from the velocity measurement to be used for comparison. The nominal mass value listed in Table 2 was utilized for the algorithm along with the motor constant identified in Section 5.1.2. A value of $k_{2_U} = 1 \times 10^5$ was selected to fulfill the gain condition given in (70) based on the expected range of operating conditions. A gain of $k_{1_U} = 2 \times 10^4$, which acts similarly to a proportional-integral gain, was selected via trial and error for optimal convergence and noise sensitivity. Similar performance was seen for values of $k_{2_U} > 7.5 \times 10^4$ and $k_{1_U} > 1 \times 10^4$ with upper limits for these gains determined by the variable limits of the real-time processor to avoid overflow.
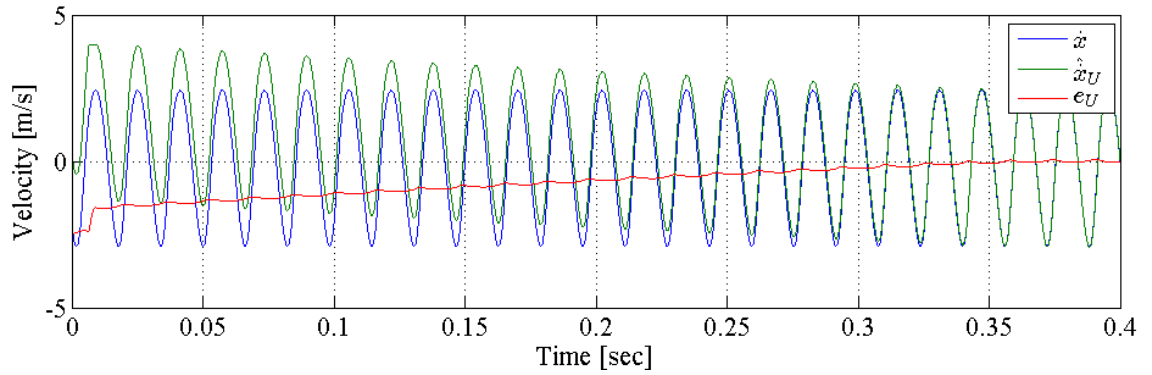
Figure 11. Comparison of velocity, measured $\dot{x}(t)$ and observed $\hat{\dot{x}}_U(t)$.
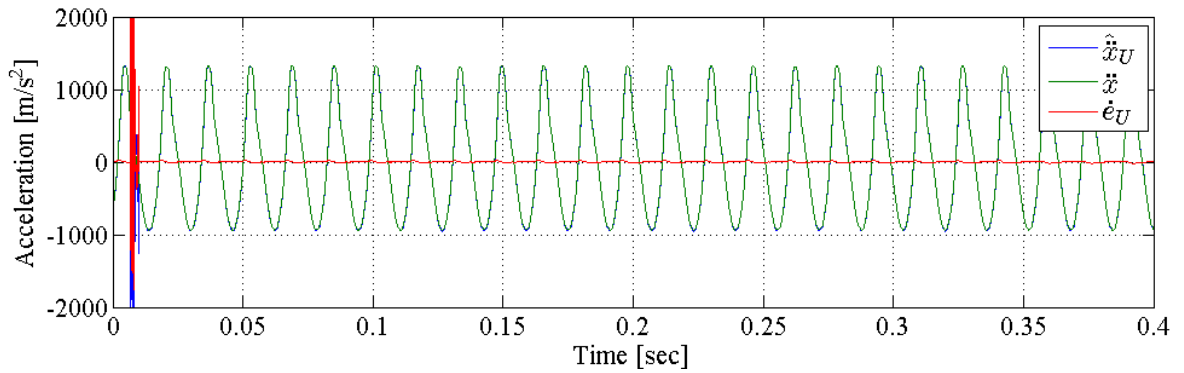
Figure 12. Comparison acceleration, measured $\ddot{x}(t)$ and observed $\hat{\dot{x}}_U(t)$.
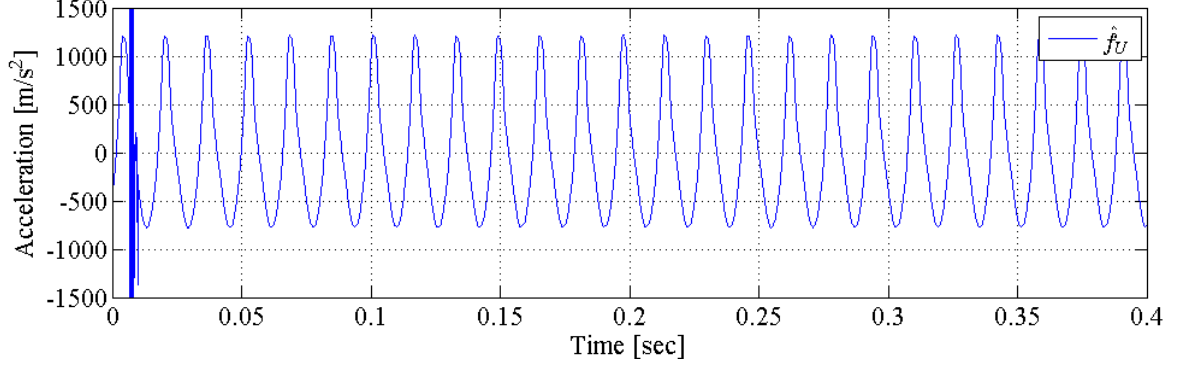
Figure 13. Uncertainty observer $\hat{f}_U(t)$.

Fig. 11-13 show the results of this experiment. Fig. 11 shows that the observed velocity converges to the actual and that observer error $e_U(t)$ is driven to zero. Fig. 12 likewise shows that the observed acceleration accurately models the measured acceleration with the ratio of the rms error, taken as a percentage of the rms of the actual acceleration, calculated as 1.21% once the observer has converged. Fig. 13 shows that the uncertainty observer is bounded, validating assertions made in the stability analysis.

6.3   TWO-STAGE OBSERVER

The goal of this observer is to combine the velocity and acceleration observers presented in the previous two subsections into a single observer which is able to observer acceleration using only a motor current measurement as well as the parameter knowledge mentioned in the previous two subsections.

6.3.1   OBSERVER DEVELOPMENT

A more practical implementation of the observers in (54) and (68) can be realized by replacing the velocity measurement required by the uncertainty observer with the output of the velocity observer defined in (55), running the two observers in parallel. This requires the error signal defined in (63) to be redefined as $e_U \triangleq \hat{\dot{x}}_V - \hat{\dot{x}}_U$. Unfortunately, it is not possible to prove stability for this implementation.

6.3.2   EXPERIMENTAL RESULTS

This scheme was tested experimentally with the same parameters and gains described previously for each observer. Once steady-state was achieved both observers were initialized at $t = 0$. Fig. 14 and 15

33

show the results of this experiment. From these figures we can see that comparable results for boundedness and convergence are obtained with this scheme as with the previous experiment, validating its use for practical application. A ratio of the rms error between the measured and observed acceleration, taken as a percentage of the rms of the actual acceleration, can be calculated as 7.56% once the observers have converged, showing that there is some loss in accuracy in comparison with the previous implementation due to the compounding of error between the two observers. There are a number of ways in which this error could be improved, primarily by improving the accuracy of the velocity observation $\hat{x}_V$. This could be accomplished by improving the fidelity and resolution of the current and voltage measurements or by taking into account the time-varying nature of the parameters L_i and α.
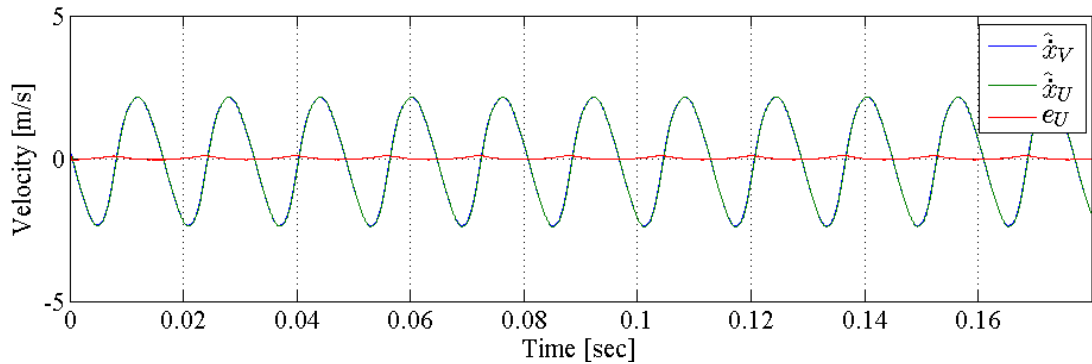
Figure 14. Velocity observers $\hat{x}_V(t)$ and $\hat{x}_U(t)$.
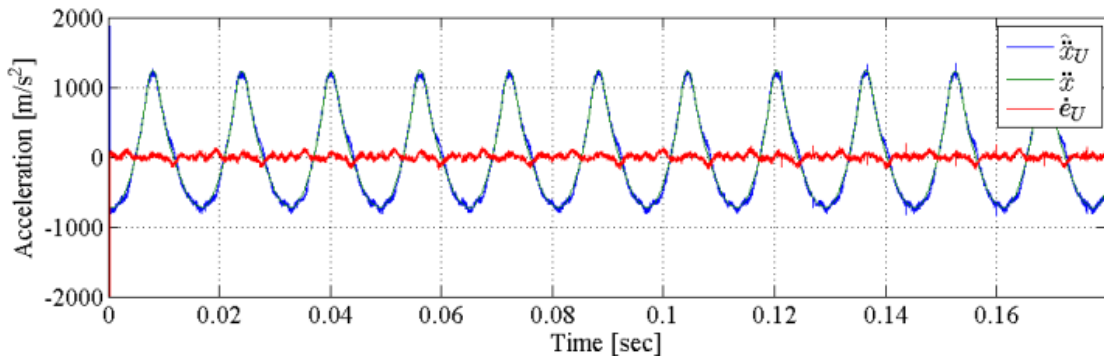
Figure 15. Comparison of acceleration, measured $\ddot{x}(t)$ and observed $\hat{\ddot{x}}_U(t)$.

6.4 GAS FORCE OBSERVER

The goal of this observer is to use measurements for motor current, piston position, and piston velocity to obtain a real-time observation for the force of gas compression. Due to the multiple mechanical

measurements necessary to implement this observer it is not suitable for production purposes. It is primarily intended as a laboratory tool for model characterization and validation.

6.4.1   OBSERVER DEVELOPMENT

A nonlinear observer is to be developed to observe the force of gas compression. To facilitate the development of this observer, the mechanical dynamics described in (2) and (3) can be combined and rewritten as

$$\ddot{x} = \frac{1}{M}[\alpha I - C\dot{x} - K(x - L_0)] + f_F \tag{71}$$

where $f_F(t) \in \mathbb{R}$ represents the scaled gas compression force term and is defined as follows:

$$f_F \triangleq \frac{1}{M}F_g. \tag{72}$$

The proceeding mathematical analysis necessitates a new set of assumptions (previous assumptions are ignored).

Assumption 1: The signals $I(t), x(t)$ and $\dot{x}(t)$ are measurable.

Assumption 2: The variables $I(t), x(t), \dot{x}(t), \ddot{x}(t), \dddot{x}(t), f_F(t), \dot{f}_F(t), \ddot{f}_F(t)$ are all piecewise continuous and bounded, hence there exist positive bounding constants $\zeta_{1_F}, \zeta_{2_F} \in \mathbb{R}^+$ such that $\left|\dot{f}_F(t)\right| < \zeta_{1_F}, \left|\ddot{f}_F(t)\right| < \zeta_{2_F}$.

Assumption 3: The machine parameters M, C, K and α are known *a priori* and are constants with respect to time.

The nonlinear observer to be designed for $f_F(t)$ is denoted as $\hat{f}_F(t) \in \mathbb{R}$ where the observer is to ensure that $\hat{f}_F(t) \rightarrow f_F(t)$ as $t \rightarrow \infty$. Utilizing $\hat{f}_F(t)$ with (71), an observed acceleration can be defined as

$$\hat{\ddot{x}}_F \triangleq \frac{1}{M}[\alpha I - C\dot{x} - K(x - L_0)] + \hat{f}_F. \tag{73}$$

Taking the integral of (73) gives the following observation for velocity:

$$\hat{\dot{x}}_F = \frac{1}{M}\int_{t_0}^{t}[\alpha I - C\dot{x} - K(x - L_0)]\, d\sigma + \int_{t_0}^{t}\hat{f}_F(\sigma)d\sigma \tag{74}$$

Utilizing (39), (40) and the observation $\hat{f}_F(t)$ the following error signals can be defined for the observer:

$$\tilde{f}_F \triangleq f_F - \hat{f}_F \tag{75}$$

$$e_F \triangleq \dot{x} - \hat{\dot{x}}_F \tag{76}$$

$$\dot{e}_F = \ddot{x} - \hat{\ddot{x}}_F \tag{77}$$

Substituting (71) and (73) into (77) and utilizing (75) gives the following relationship between $\dot{e}_F(t)$ and $\tilde{f}_F(t)$:

$$\dot{e}_F = \tilde{f}_F. \tag{78}$$

A filtered error signal $s_F(t)$ is defined as

$$s_F \triangleq \dot{e}_F + e_F. \tag{79}$$

From the subsequent stability analysis the following observer is designed for the uncertainty signal:

$$\dot{\hat{f}}_F \triangleq (k_{1_F} + 1)s_F + k_{2_F}sgn(e_F) \tag{80}$$

where $k_{1_F}, k_{2_F} \in R^+$ are constant gains. The dependence of (80) on $s_F(t)$ makes it unrealizable per Assumption 7. A realizable from of $\hat{f}_F(t)$ can be obtained by substituting (79) into (80) and integrating both sides of the resulting equation to obtain the following:

$$\hat{f}_F = (k_{1_F} + 1)\left[e_F(t) - e_F(t_0) + \int_{t_0}^{t} e_F(\sigma)d\sigma\right] + k_{2_F}\int_{t_0}^{t} sgn(e_F(\sigma))d\sigma + \hat{f}_F(t_0). \tag{81}$$

Remark 6.4.1: Due to the dependence of this observer on position and velocity measurements, it is not useful for production-level applications, but may still be of interest for laboratory characterization of the gas force where full state measurements are available.

Remark 6.4.2: The stability analysis presented in the appendix proves that the nonlinear observer $\hat{f}_U(t)$ defined in (81) converges to the uncertainty signal $f_U(t)$.

6.4.2   STABILITY ANALYSIS

Theorem 6.4.1: The observer defined in (81) ensures that

$$\hat{f}_U(t) \rightarrow f_U(t) \quad as \quad t \rightarrow \infty \tag{82}$$

provided that the observer gain k_{2_U} is selected to meet the following sufficient condition:

$$k_{2_U} > \zeta_{1_U} + \zeta_{2_U}. \tag{83}$$

Proof: See Appendix.

6.4.3   EXPERIMENTAL RESULTS

A sinusoidal voltage excitation was applied to the motor with a peak of 194 [V] and a frequency of 62.3 [Hz]. The nozzle was adjusted to bring the discharge pressure of the compressor to 120 [psi]. The nominal mass, friction coefficient, and spring constant values listed in Table 2 were utilized for the algorithm along with the motor constant identified in Section 5.1.2. For the observer gain values of $k_{1_F} = 2 \times 10^4$, $k_{2_F} = 1 \times 10^5$ were selected to meet the requirements stated in (83). With the system operating at steady-state the observer algorithm was turned on at $t = 0$. Figures 16 and 17 show the results of the experiment. Fig. 16 shows that the observed velocity converges to the measured and that observer error $e_F(t)$ is driven to zero. Fig. 17 shows that the observed gas force is bounded. Without some sort of sensor to measure gas force we have no reference signal with which to determine accuracy.
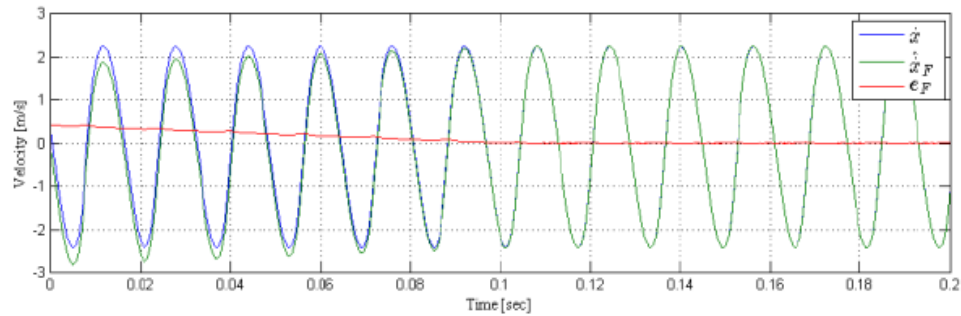

Figure 16. Comparison of actual velocity $\dot{x}(t)$ and observed velocity $\hat{\dot{x}}_F(t)$.
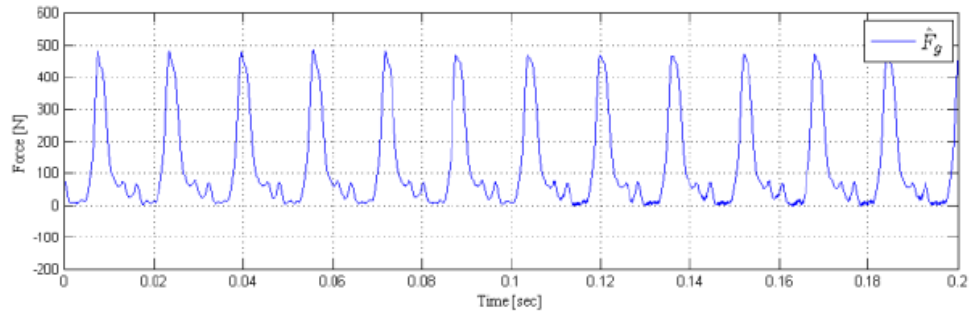
Figure 17. Observed gas force $\hat{F}_g(t)$.

37

6.5 POSITION AND PRESSURE OBSERVER

The goal of this observer is to obtain real-time observations for both the absolute piston position as well as the suction and discharge pressures. Through this development several other signals are also incidentally observed such as the gas compression force and the piston acceleration. Whereas the observers developed for these signals in sections 6.2 and 6.4, respectively, assumed bounded time-varying uncertainties for the unmodeled terms, this observer development seeks to fully model all terms in the mechanical dynamics and reduce all uncertainties to parametric uncertainties. With an observer form which has only parametric uncertainties an adaptive update law can be designed to account for these.

6.5.1 RELATIVE POSITION OBSERVER

Looking at the mechanical dynamic equations (2) and (3) we can see that the acceleration is dependent upon the absolute piston position $x(t)$ via the spring force term. This feedback gives us an opportunity to observe the position via its effects on the mechanical dynamics. Assuming that we have an accurate velocity observation from Section 6.1, it is natural to approximate the absolute position by integrating this signal. Unfortunately, this method is not reliable for obtaining an absolute position observation in practical implementation. This is due to the fact that an artificial DC bias is propagated into the velocity observation from the input voltage bias of the non-ideal analog to digital converter (ADC) which is used to obtain the current measurement $I(t)$. Looking at (46), we can see that in order to satisfy $\hat{I}(t) \rightarrow I(t)$ the scaled velocity observer $\hat{f}_V(t)$ must assume a DC offset to cancel out the bias present in the $I(t)$ term of the same equation. This DC offset propagates into the velocity observation per the definition in (55).

Because of this offset in $\hat{x}_V(t)$ we can see that the observed position defined in (84) will become positively or negatively unbounded depending on the sign of the DC offset. In reality, even a measured velocity will have some finite inaccuracy which over time will cause drift in the integrator. Though this offset may be measured and compensated for it can never be fully cancelled out without some form of high

pass filtering. High pass filtering would have the undesirable effect of removing any real DC component from the velocity signal which we know occurs during transient periods where the gas compression force, $F_g(t)$ is changing the midstroke of the piston.

Thus to make use of this integrated signal we must find a way to artificially bound it. A method is proposed whereby the integral is reset to a value of zero each time the piston reaches top dead center x_{TDC}. As top dead center represents the minimum point in the piston position we can identify this point in the cycle by looking at when the velocity signal experiences a positive-going zero cross. The time of the most recent of these occurrences is denoted as $\hat{t}_{TDC}$. A relative position signal $\bar{x}(t)$ defined using this periodic resetting can thus be defined as

$$\bar{x}(t) \triangleq \int_{\hat{t}_{TDC}}^{t} \hat{x}_V(\sigma) d\sigma. \tag{84}$$

We can see that by resetting the integrator to zero at each $\hat{t}_{TDC}$ the resulting signal $\bar{x}(t)$ will have a minimum value of zero. This methodology assumes that the bias accumulated over each cycle from the velocity is negligible and does not result in significant discontinuities at the time of resetting. From this assumption we can treat the signal $\bar{x}(t)$ as a shifted version of the absolute piston position $x(t)$, where the value by which the signal has been shifted is equal to x_{TDC}.

$$\bar{x}(t) = x(t) - x_{TDC} \tag{85}$$

Assuming that x_{TDC} is slowly time-varying, which is a valid assumption under steady-state conditions, gives us the ability to use adaptive methods to estimate this value.

6.5.2   LINEARLY PARAMETERIZED GAS FORCE

In order to fully model the mechanical dynamics we also require a structured form of the unknown time-varying gas force $F_g(t)$. Fortunately, we have such a form given in Table 1. Unfortunately, many of the parameters within this piecewise equation are unknown. However, we can rewrite this equation in a linearly parameterized form such that the gas force $F_g(t)$ is equal to the inner product of a vector of known time-varying regressors $W(t) \in \mathbb{R}^{1 \times 2}$ and a vector of unknown constant parameters $\theta \in \mathbb{R}^{2 \times 1}$ as shown:

$$F_g = A_p W \theta. \tag{86}$$

From this we can then use adaptive methods to estimate the unknown parameters comprising θ. In this case θ consists of the unknown constant suction and discharge pressures, i.e. $\theta \triangleq [P_s \quad P_d]^T$, and the piecewise regressor terms comprising $W(t) \triangleq [W_1 \quad W_2]$ are defined in Table 3 below.

Table 3

Regressor Variable Definitions for Piecewise Gas Force

Stage	Piecewise Condition	W_1	W_2
Compression [1] − [2]	$\dot{x} < 0,$ $P(t) < P_d$	$\left[\left(\frac{x_{BDC}}{x(t)}\right)^n - 1\right]$	0
Discharge [2] − [3]	$\dot{x} < 0,$ $P(t) \geq P_d$	-1	1
Decompression [3] − [4]	$\dot{x} > 0,$ $P(t) > P_s$	-1	$\left(\frac{x_{TDC}}{x(t)}\right)^n$
Suction [4] − [1]	$\dot{x} > 0,$ $P(t) \leq P_s$	0	0

We can see that by substituting this definition of $W(t)$ into (86), we obtain the same definition for gas force $F_g(t)$ given in Table 1.

6.5.3   OBSERVER DEVELOPMENT

An observer is to be designed for the mechanical dynamics of the compressor. To facilitate the development of this observer, the mechanical dynamics described in (2) and (3) can be combined and substitutions made using (85) and (86) to obtain the following:

$$\ddot{x} = \frac{1}{M}\left[\alpha I + A_p W\theta - C\dot{x} - K(\bar{x} + x_{TDC} - L_0)\right] \tag{87}$$

The subsequent development necessitates the following set of assumptions for this model:

Assumption 1: The signals $I(t)$, and $\dot{x}(t)$ are known.

Assumption 2: The variables $I(t), x(t), \dot{x}(t), F_g(t)$ are all piecewise continuous and bounded.

Assumption 3: The machine parameters M, C, K, A_p, n and α are known *a priori* and are constants with respect to time.

Assumption 4: The unknown parameters P_s, P_d, x_{TDC} are bounded and slowly time-varying such that $\dot{P}_s, \dot{P}_d, \dot{x}_{TDC} \approx 0$.

As mentioned in Assumption 1 a velocity signal $\dot{x}(t)$ is required. It is to be understood that this signal can be replaced with the observer $\hat{x}_V(t)$ from Section 6.1 to make the resulting observer sensorless in a similar way as was done in Section 6.3 with the acceleration observer.

To avoid the need for a position measurement the subsequent development uses the relative position $\bar{x}(t)$ defined in (84) instead, accounting for the fact that it is shifted from the absolute position. From this the following error signal can be defined for our observer $\hat{x}(t)$:

$$\tilde{x} \triangleq \bar{x} - \hat{x} \tag{88}$$

Substituting (85) into (88) and taking the time derivative, noting Assumption 4, we obtain the following velocity error signal for the observer:

$$\dot{\tilde{x}} = \dot{x} - \dot{\hat{x}} \tag{89}$$

To facilitate the development a filtered error signal $r(t) \in \mathbb{R}$ is defined as

$$r \triangleq \dot{\tilde{x}} + k_1 \tilde{x} \tag{90}$$

where $k_1 \in \mathbb{R}$ is a positive filter gain. Note that because $\dot{x}(t)$ is known, both $\dot{\tilde{x}}(t)$ and $r(t)$ are realizable signals. Taking the time derivative of (90) and substituting in (87) we obtain the following open loop error dynamics:

$$\dot{r} = \frac{1}{M}\left[\alpha I + A_p W\theta - C\dot{x} - K(\bar{x} + x_{TDC} - L_0)\right] - \ddot{\hat{x}} + k_1\dot{\tilde{x}}. \tag{91}$$

Motivated by the form of (91) and the subsequent stability analysis the observer $\ddot{\hat{x}}(t)$ is designed as

$$\ddot{\hat{x}} \triangleq \frac{1}{M}\left[\alpha I + A_p W\hat{\theta} - C\dot{x} - K(\bar{x} + \hat{x}_{TDC} - L_0)\right] + k_1\dot{\tilde{x}} + \tilde{x} + k_2 r \tag{92}$$

where $k_2 \in \mathbb{R}$ is a positive control gain, and $\hat{\theta}(t), \hat{x}_{TDC}(t) \in \mathbb{R}$ are parameter estimates defined by the following adaptive update laws:

$$\dot{\hat{\theta}} \triangleq \frac{A_p}{M}\Gamma W^T r \tag{93}$$

$$\dot{\hat{x}}_{TDC} \triangleq -\frac{k_x K}{M}r \tag{94}$$

where $\Gamma \in \mathbb{R}^{2\times2}$ is a positive diagonal gain matrix defined as $\Gamma \triangleq k_P I_2$ ($k_P \in \mathbb{R}$ being a positive gain) and $k_x \in \mathbb{R}$ is a positive estimator gain. Error terms for these estimates are defined as

$$\tilde{\theta} \triangleq \theta - \hat{\theta} \tag{95}$$

$$\tilde{x}_{TDC} \triangleq x_{TDC} - \hat{x}_{TDC}. \tag{96}$$

Substituting (92) into (91) we obtain the following closed loop error dynamics for the proposed observer:

$$\dot{r} = -k_2 r - \tilde{x} + \frac{1}{M}\left[A_p W \tilde{\theta} - K \tilde{x}_{TDC}\right]. \tag{97}$$

Remark 6.5.1: The proposed implementation requires knowledge of $W(t)$ per the definitions in (92),(93). However, we can see from Table 3 that $W(t)$ depends upon the terms $x(t), x_{TDC}, x_{BDC}$, which are not available in a sensorless implementation. As such, for a sensorless implementation we are forced to substitute observed values for each of these terms. Motivated by (85) we substitute $\bar{x}(t) + \hat{x}_{TDC}$ for $x(t)$, $\hat{x}_{TDC}$ for x_{TDC}, and $\bar{x}(\hat{t}_{BDC}) + \hat{x}_{TDC}$, where $\hat{t}_{BDC}$ is the most recent time at which the piston reached bottom dead center as determined by the negative-going zero-crossing of the velocity signal. Moreover, the piecewise conditions listed in Table 3 are also dependent upon the unknown pressures. In this case as well we are forced to use the estimated pressures $\hat{P}_s, \hat{P}_d$ resulting from $\hat{\theta}(t)$ in place of the actual pressures P_s, P_d. From the relationship between $P(t)$ and $F_g(t)$ given in (1) and Table 1 we can define the following observer $\hat{P}(t)$ to be used in the piecewise conditions for $W(t)$:

$$\hat{P}(t) \triangleq (W_1 + 1)\hat{P}_s + W_2 \hat{P}_d. \tag{98}$$

With these substitutions we introduce a recursive feedback into the observer. As this feedback is not modeled in the development presented in this section the subsequent stability analysis cannot be used to prove that the closed loop system is stable under these substitutions. Thus it is left to experimental validation to show whether the proposed sensorless method is stable and convergent.

6.5.4   STABILITY ANALYSIS

Theorem 6.5.1: The closed loop system defined by the observer in (92) and estimators in (93), (94) together ensure that the observer errors $\tilde{x}(t), r(t) \to 0$ as $t \to \infty$.

Proof: A non-negative Lyapunov function $V(t)$ is defined for the closed loop system as

$$V \triangleq \frac{1}{2}\tilde{x}^2 + \frac{1}{2}r^2 + \frac{1}{2}\tilde{\theta}^T \Gamma^{-1}\tilde{\theta} + \frac{1}{2k_x}\tilde{x}_{TDC}^2. \tag{99}$$

Taking the time derivative of (99) we obtain the following:

$$\dot{V} = \tilde{x}\dot{\tilde{x}} + r\dot{r} + \tilde{\theta}^T \Gamma^{-1}\dot{\tilde{\theta}} + \frac{1}{k_x}\tilde{x}_{TDC}\dot{\tilde{x}}_{TDC}. \tag{100}$$

Then solving (90) for $\dot{\tilde{x}}(t)$ and substituting this and the closed loop error dynamics from (97) into (100), and also substituting in the time derivatives of (95), (96), taking into account that $\dot{P}_s, \dot{P}_d, \dot{x}_{TDC} \approx 0$, we obtain:

$$\dot{V} = \tilde{x}(r - k_1\tilde{x}) + r\left(-k_2 r - \tilde{x} + \frac{1}{M}\left[A_p W\tilde{\theta} - K\tilde{x}_{TDC}\right]\right) - \tilde{\theta}^T \Gamma^{-1}\dot{\tilde{\theta}} - \tag{101}$$

$$\frac{1}{k_x}\tilde{x}_{TDC}\dot{\hat{x}}_{TDC}.$$

Simplifying (101) and substituting into it (93) and (94) we obtain the following:

$$\dot{V} = -k_1\tilde{x}^2 - k_2 r^2 + \frac{1}{M}r\left(A_p W\tilde{\theta} - K\tilde{x}_{TDC}\right) - \frac{A_p}{M}W\tilde{\theta}r - \frac{K}{M}\tilde{x}_{TDC}r. \tag{102}$$

Simplifying (102) we obtain the final result

$$\dot{V} = -k_1\tilde{x}^2 - k_2 r^2. \tag{103}$$

From the form of (99) and (105) it is clear that $\tilde{x}(t), r(t), \tilde{\theta}(t), \tilde{x}_{TDC}(t) \in \mathcal{L}_\infty$ and that $\tilde{x}(t), r(t) \in \mathcal{L}_\infty \cap \mathcal{L}_2$. From (90) and the fact that $\tilde{x}(t), r(t) \in \mathcal{L}_\infty$ we can see that $\dot{\tilde{x}}(t) \in \mathcal{L}_\infty$.

To prove boundedness of $\dot{r}(t)$ we must first show that $W(t) \in \mathcal{L}_\infty$. This analysis will consider only cases where $x(t) \geq 0$. Cases where $x(t) < 0$ require a modification of the algorithm which is discussed in Section 6.5.7. Looking at the individual terms W_1, W_2 we can see that by definition both terms are constants during all stages of the compression cycle, except for W_1 during compression and W_2 during decompression. Looking at W_1 during compression we can see that as $x(t) \to 0$, $W_1(t) \to \infty$. However, from (98) we can see that as $W_1(t) \to \infty$, $\hat{P}(t) \to \infty$ as well, meaning that the piecewise condition $\hat{P}(t) \geq \hat{P}_d$ will always be met before $x(t) = 0$ for bounded $\hat{P}_d$. From Assumption 4 and the fact that $\tilde{\theta}(t) \in \mathcal{L}_\infty$ we can see that $\hat{P}_s, \hat{P}_d \in \mathcal{L}_\infty$. Thus $W_1(t)$ will always transition into the discharge stage before $x(t) = 0$, giving it an upper bound of $\hat{P}_d/\hat{P}_s$. For W_2 during decompression we again see that the term is problematic as $x(t) \to 0$. However if we consider the assumption that $x(t) \geq 0$, then $x(t)$ can equal zero if and only if it is at a local minimum, meaning that $x_{TDC} = 0$. Substituting this value into the definition of W_2 and taking the limit as $x(t) \to 0$ we see that $W_2 = 0$. For any non-zero value of $x(t)$ we can see that W_2 is

bounded so long as x_{TDC} is bounded, which was given in Assumption 4. Thus we have shown that $W_1, W_2 \in \mathcal{L}_\infty$.

From (97) and the fact that $\tilde{x}(t), r(t), \tilde{\theta}(t), \tilde{x}_{TDC}(t), W(t) \in \mathcal{L}_\infty$ we can see that $\dot{r}(t) \in \mathcal{L}_\infty$. Since $\tilde{x}(t), r(t) \in \mathcal{L}_\infty \cap \mathcal{L}_2$ and $\dot{\tilde{x}}(t), \dot{r}(t) \in \mathcal{L}_\infty$ Barbalat's Lemma [23] can be utilized to prove that $\tilde{x}(t), r(t) \to 0$ as $t \to \infty$.

6.5.5   EXPERIMENTAL RESULTS

The model parameters listed in Table 2 were utilized for this experiment along with the following observer gains and initial values: $k_1 = 100, k_2 = 1000, k_P = 400, k_x = 0.05, \hat{P}_s(t_0) = 20 \, [psi], \hat{P}_d(t_0) = 50 \, [psi], \hat{x}_{TDC}(t_0) = 4 \, [mm]$. The system was driven under current control with a fixed amplitude of $0.6 \, [A]$ and a driving frequency of $45.7 \, [Hz]$. The scheme was implemented in a fully sensorless manner, meaning that the velocity signal used in (84) and (89) comes from the sensorless velocity observer developed in Section 6.1.

Figures 18-20 show the transient performance of the observer signals $\hat{x}(t), \dot{\hat{x}}(t)$ during the initial observer convergence. We can see from Figures 18 and 19 that within two cycles both of these signals converge to their respective reference signals $\bar{x}(t), \dot{x}(t)$ and thus in Figure 20 that the observer error signals $\tilde{x}(t), \dot{\tilde{x}}(t), r(t)$ are quickly regulated. We see that there is some residual component of the error $r(t)$ owing to the fact that the parameter estimates $\hat{x}_{TDC}, \hat{P}_s, \hat{P}_d$ have not fully converged within this time period.

Figures 21 and 22 show the convergence of these parameter updates, which take place over a much longer time scale. From these figures we can see that not only are these parameters convergent, but that they display a high level of accuracy when compared to their measured counterparts. In Figure 23-25 we can see the performance of the observer after the parameters have converged and the observer is operating at steady-state. Figure 23 shows the total position observer consisting of the relative position observer $\bar{x}(t)$ and the top dead center estimate $\hat{x}_{TDC}$. This absolute position observer is shown in comparison with the actual measured piston position $x(t)$. From this we can see the high level of accuracy achieved by the

44

adaptive observer. Figures 24 and 25 show the steady-state results of the pressure and gas force estimation. In Figure 24 we see the instantaneous chamber pressure observer $\hat{P}(t)$ derived from (99) along-side the pressure estimates $\hat{P}_s, \hat{P}_d$, showing the movement of the observer through the four compression cycle stages. Figure 25 shows the resulting gas force observer $\hat{F}_g(t)$. Unfortunately, since measurements of internal pressures and forces are difficult to obtain we have no means of judging the accuracy of the two observer signals $\hat{P}(t)$ and $\hat{F}_g(t)$.
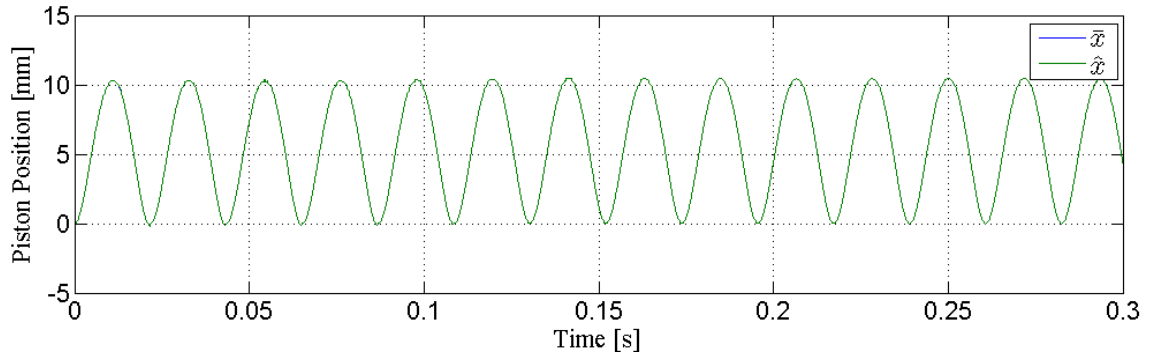
Figure 18. Comparison of relative position signal $\bar{x}(t)$ and observer position signal $\hat{x}(t)$ during initial transient.
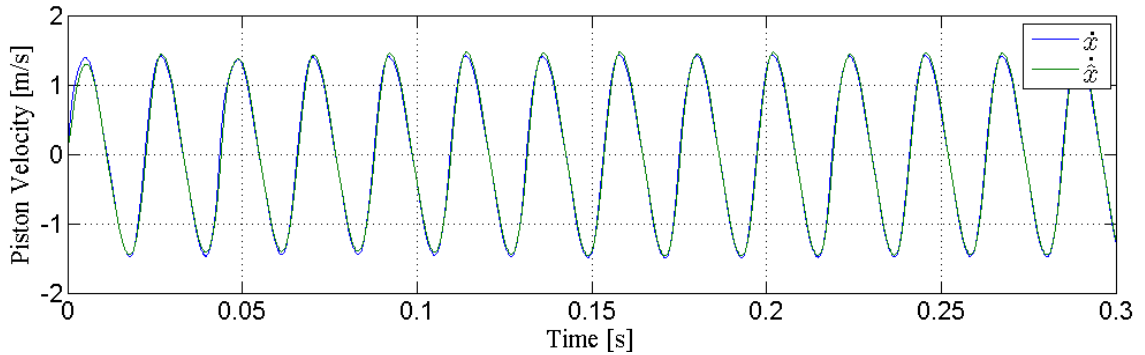
Figure 19. Comparison of velocity signal $\dot{x}(t)$ and observer velocity $\dot{\hat{x}}(t)$ during initial transient.
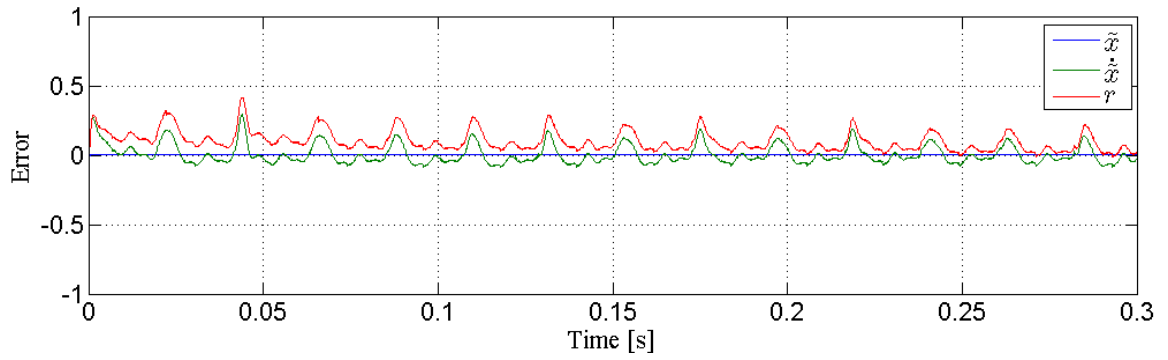
Figure 20. Convergence of observer error signals $\tilde{x}(t), \dot{\tilde{x}}(t), r(t)$ during initial transient.
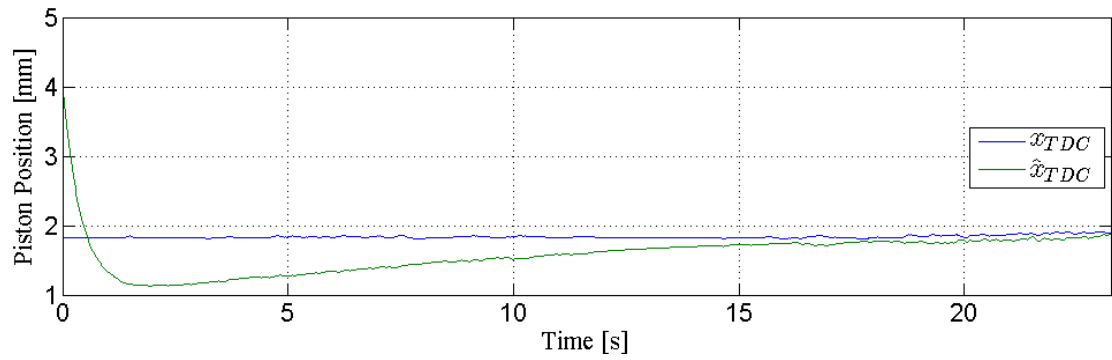
Figure 21. Convergence of parameter estimate $\hat{x}_{TDC}$ to actual top dead center value x_{TDC}.
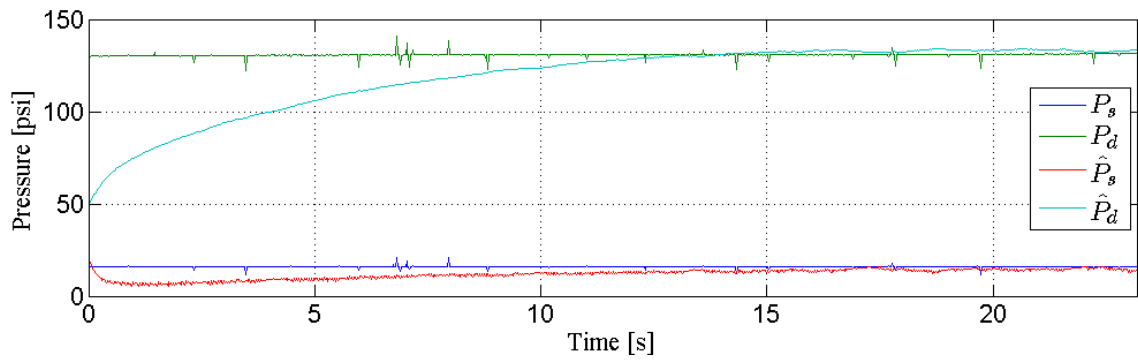
Figure 22. Convergence of parameter estimates $\hat{P}_s, \hat{P}_d$ to actual pressures P_s, P_d.
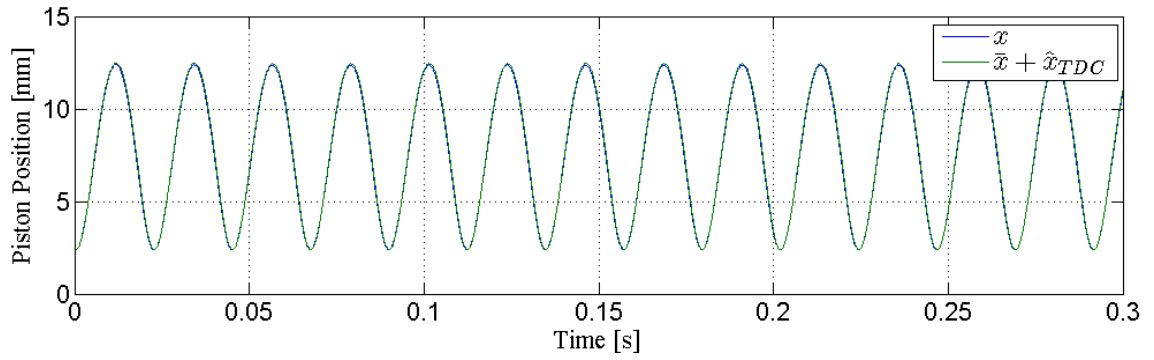
Figure 23. Comparison of position observer including top dead center estimate ($\bar{x}(t) + \hat{x}_{TDC}$) with actual absolute position $x(t)$ under observer steady-state.
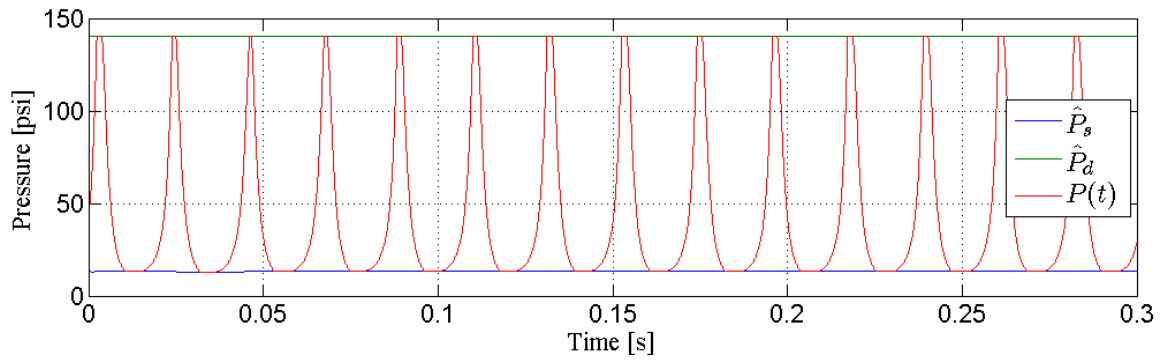
Figure 24. Instantaneous chamber pressure observer $\hat{P}(t)$ during observer steady-state, shown with estimated suction and discharge pressures $\hat{P}_s, \hat{P}_d$.
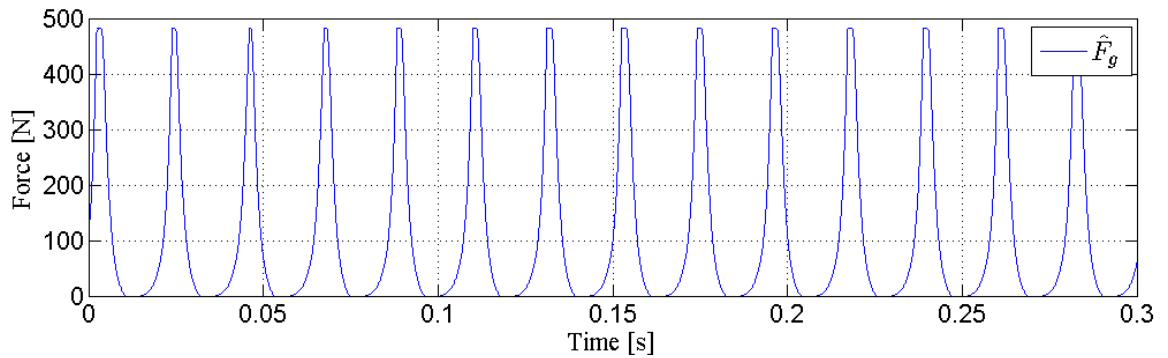
Figure 25. Instantaneous gas force observer $\hat{F}_g(t)$ during observer steady-state as calculated from estimated pressures $\hat{P}_s, \hat{P}_d$.

6.5.6   INCOMPLETE CYCLE MODIFICATION

The gas force model presented in Section 2.1 and utilized in Section 6.5.2 is based upon the assumption that the compression cycle passes through all four stages in order: compression, discharge, decompression, suction. It is this assumption that allows us to assume that the chamber pressure $P(t)$ at the beginning of the compression stage is equal to P_s and thus relate the gas force to P_s via the W_1 term for that stage. Similarly, we assume that at the beginning of the decompression stage that $P(t)$ is equal to P_d, which allows us to relate the gas force to P_d via the W_2 term for that stage.

However, during startup and shutdown conditions it is likely that the piston stroke is not large enough to reach the piecewise pressure conditions necessary to enter the discharge and suction stages of the compression cycle resulting in an incomplete cycle. For instance, if $P(t)$ does not exceed P_d during the compression stage then the system will skip the discharge stage and move directly into the decompression stage, but instead of beginning that stage at P_d, it will begin it at whatever pressure the compression stage ended. Similarly, if $P(t)$ does not decrease to P_s during the decompression stage then the system will skip the suction stage and move directly into the compression stage starting at whatever pressure the decompression stage ended instead of P_s.

For both of these cases the algorithm must be modified to reflect this reality, otherwise the resulting $P(t)$ and $F_g(t)$ will be discontinuous at these stage transitions causing instability in the observer. To remedy this, whenever the observer enters either the compression or decompression stage it checks to see which stage it just left. If this reveals that a discharge or suction stage was skipped then the algorithm uses the last value of $P(t)$ in place of P_s or P_d (for compression and decompression stages, respectively) in the θ vector. Also, since $P(t)$ is no longer dependent on P_s or P_d during this stage, the associated update $\dot{\hat{\theta}}$ is forced to be zero for the duration of the stage. This is meant to prevent runaway conditions where the estimator would attempt to reduce error $r(t)$ by updating $\hat{P}_s$ or $\hat{P}_d$ via (93), (94), but since the respective term is no longer affecting the estimated gas force, there is no feedback whereby it can reduce the error, causing it to runaway during that time.

These modifications are relatively easy to implement, but are difficult to express in a closed form, and thus cannot be proven to maintain stability via the analysis given in Section 6.5.4.

6.5.7 SOFT CRASH MODIFICATION

Another instance in which the gas force model presented in Section 2.1 is violated is under the soft crash condition. Soft crashing is the result of the compressor piston being overdriven, causing it to come into physical contact with the discharge valve as shown in Figure 26. Here, the piston shown in red, extends past the end of the compression cylinder, shown in green, causing it to come into contact with the discharge valve shown in grey.
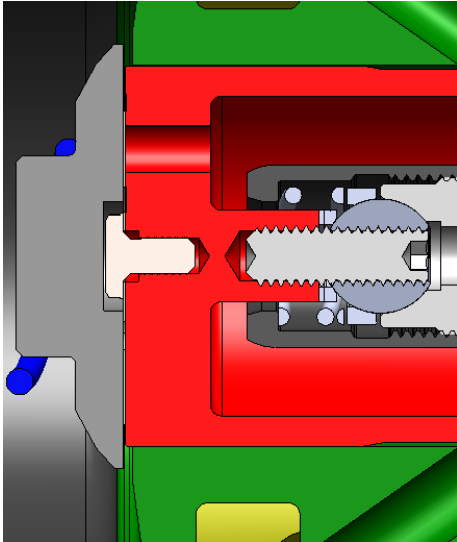
Figure 26. Example of soft crash condition for linear compressor.

The cylinder head, which corresponds to the far left extremity of the compression cylinder shown in Figure 26, is defined as the reference position $(x = 0)$ of the piston because at this point the compression chamber volume is theoretically equal to zero. Thus when the piston extends past this point the piston position becomes negative. Given the model from Section 2.1 this would imply a negative volume, which is of course impossible, we are forced to modify the model and the subsequent observer design to ensure accurate modeling of soft crash conditions.

From Figure 26 we can see that the presence of the discharge valve causes the volume of the compression chamber to remain equal to zero until the piston has withdrawn past the head and come out of contact with the discharge valve. We can also see that because the pressure on the back-side of the discharge valve is by definition P_d, that during this period the effective chamber pressure $P(t)$ (as it effects the gas force) will still be equal to P_d, even though technically there is no gas in the compression chamber. Another important fact to note is that in order for the compression volume to reach zero, as it must before

soft crashing, the chamber pressure will by necessity exceed P_d. We can infer this from the form of chamber pressure expression given for the compression stage in Table 1. Since $x(t)$ is in the denominator of this expression, we can see that as $x(t) \to 0, P(t) \to \infty$. Thus any finite discharge pressure P_d will be exceeded before $x(t) = 0$, resulting in transition to the discharge stage of the cycle. This means that the stage of the cycle at the time of soft crashing will always be the discharge stage.

Therefore, since the compressor is in discharge stage before soft crashing, and since the effective chamber pressure during soft crashing is P_d, which is the same as in the discharge stage, we can accurately model the effect of soft crashing on gas force by keeping the compressor in the discharge stage during this condition. This can be easily done by redefining the piecewise condition which determines transition from the discharge to the decompression stage. By forcing the model to wait until $x > 0$ before beginning decompression we are able to obtain the desired effect. One point that remains to be defined is the value of x_{TDC} to be used in the W_2 expression in Table 3 during the decompression stage. As previously defined, x_{TDC} corresponds to the minimum position of the piston. However, since during soft crashing this is a negative value and would thus imply negative volume, we need to make some modification. Forcing x_{TDC} to be equal to zero in this case makes sense as this would reflect the reality that the volume is beginning the decompression stage at zero, however from the decompression expression for W_2 we see that this would cause W_2 to be zero, meaning that $P(t)$ would immediately transition from P_d to zero, causing transition immediately to the suction stage. While this is not necessarily incorrect for a theoretical model, to give the observer continuity a small positive constant $\varepsilon \in \mathbb{R}$ is utilized instead, resulting in a very short but still continuous decompression stage. In order to prevent conditions where $W_2 > 1$ during decompression, we also use ε as the boundary condition (instead of $x = 0$) for entering the decompression stage. A revised version of the regressor definitions given in Table 3 with piecewise conditions which have been modified to account for soft crash conditions is shown in Table 4 below. We can see that these modified definitions of W_1, W_2 maintain the boundedness required by the stability analysis.

Table 4

Revised Regressor Variable Definitions for Piecewise Gas Force

Stage	Piecewise Condition	W_1	W_2
Compression [1] − [2]	$\dot{x} < 0 \mid x \leq \varepsilon,$ $P(t) < P_d$	$\left[\left(\frac{x_{BDC}}{x(t)}\right)^n - 1\right]$	0
Discharge [2] − [3]	$\dot{x} < 0 \mid x \leq \varepsilon,$ $P(t) \geq P_d$	-1	1
Decompression [3] − [4]	$\dot{x} > 0 \;\&\; x > \varepsilon$ $P(t) > P_s$	-1	$\left(\frac{x_{TDC}}{x(t)}\right)^n$
Suction [4] − [1]	$\dot{x} > 0 \;\&\; x > \varepsilon,$ $P(t) \leq P_s$	0	0

7 PER-CYCLE OBSERVATIONS

To achieve the system level control objectives of resonance-tracking and stroke control it is necessary to derive auxiliary observations of system-level states from the instantaneous observer signals obtained in Sections 6. Specifically, two per-cycle signals are needed for the desired control, the relative phase between velocity and current, and the piston top dead center value x_{TDC}. A method for estimating x_{TDC} has already been provided in Section 6.5, however for thoroughness an alternate derivation based on earlier methodologies is presented in Section 7.4. This method requires observations for the piston stroke length Δx_{SL} and bottom dead center x_{BDC} which are derived in the preceding sections. The accuracies of these observations is directly related to the accuracy of the two-stage observer presented in Section 6.4 which has already been demonstrated in Section 6.4.3. Similarly, the phase observation derived in Section 7.1 is directly related to the velocity observer developed in Section 6.1. As such independent experimental validations are not provided for these per-cycle observations, however, the results in Section 8.5, which utilize these observations can be referenced for this purpose.

7.1 PHASE OBSERVATION

Per the definition of resonance given in Section II the relative phase difference between the piston velocity and the motor force, which per (3) has the same phase as the motor current, can be used as an indicator of whether the system is operating at its resonance frequency [14], [15]. Utilizing the observed velocity from (55), an observed phase can be obtained by comparing the zero-crossing of this signal with that of the measured current. At the time of a positive zero-crossing in $\hat{x}_V(t)$, the elapsed time since the most recent positive zero-crossing in $I(t)$ is calculated and denoted as Δt. From Δt a phase observation $\hat{\theta}_{VI}$ in degrees can be defined as

$$\hat{\theta}_{VI} \triangleq 360 \cdot \Delta t \cdot f \tag{104}$$

where $f \in \mathbb{R}$ is the fundamental frequency of the system. Standard phase wrapping can be used to shift the domain of $\hat{\theta}_{VI}$ from $[0°, 360°)$ to $(-180°, 180°]$, which is more desirable for control purposes. Per this measurement methodology a new phase observation is obtained once per cycle. It should be noted that this calculation of relative phase is used for ease of implementation as zero-crossings are easily detectable. In reality, because of the nonlinear gas force, the velocity and current signals will contain multiple harmonics each with their own relative phase.

7.2   STROKE LENGTH OBSERVATION

As defined in (4), the stroke length is equal to the distance traveled between top dead center (the minimum position of the piston stroke) and bottom dead center (the maximum position of the piston stroke). Given that the relative position signal $\bar{x}(t)$ defined in (85) is equal to zero at top dead center, we can see that at bottom dead center it will be equal to the stroke length of the observed position. Bottom dead center time can be identified by the negative-going zero-crossing of the observed velocity $\hat{\dot{x}}_V(t)$, similar to how the timing of top dead center was identified in Section 6.5.1. The time of the most recent of these occurrences is denoted as $\hat{t}_{BDC}$. Thus observed stroke length can be defined as

$$\Delta \hat{x}_{SL} \triangleq \bar{x}(\hat{t}_{BDC}). \tag{105}$$

From this we can see that a new value for $\Delta \hat{x}_{SL}$ is obtained only once per cycle.

7.3   BOTTOM DEAD CENTER OBSERVATION

A scheme similar to the one proposed in [6] is used for estimation of the bottom dead center based on the developed velocity and acceleration observers. From Fig. 2 we can see that at t_{BDC} the chamber pressure is equal to the suction pressure, which from (1) shows that $F_g(t_{BDC}) = 0$. Likewise, since bottom dead center is by definition a local maximum of the position it can be seen that $\dot{x}(t_{BDC}) = 0$ as well, and assuming convergence of the velocity observer that $\hat{\dot{x}}_V(\hat{t}_{BDC}) = 0$ as well. Using this information the mechanical dynamics of the system (2) and (3) at this instant of time can be simplified as

$$\alpha I(t_{BDC}) = M\ddot{x}(t_{BDC}) + K(x_{BDC} - L_0). \tag{106}$$

Rewriting (106) and substituting the observed acceleration from the defined in (21) and the estimated

bottom dead center timing $\hat{t}_{BDC}$ a bottom dead center observation can be defined as

$$\hat{x}_{BDC} \triangleq \frac{1}{K}\left(\alpha I(\hat{t}_{BDC}) - M\hat{\ddot{x}}_U(\hat{t}_{BDC})\right) + L_0. \tag{107}$$

Note that a new value of $\hat{x}_{BDC}$ can be calculated whenever $t = t_{BDC}$, i.e. once per cycle.

7.4   TOP DEAD CENTER OBSERVATION

An observation for top dead center can be obtained by rewriting (4) and substituting the stroke length and

bottom dead center observations defined in (105) and (107), respectively, to obtain the following

$$\hat{x}_{TDC} \triangleq \hat{x}_{BDC} - \Delta\hat{x}_{SL}. \tag{108}$$

8   REGULATION CONTROLLERS

Three different levels of control are proposed to achieve the system level control objectives of resonance-tracking and stroke control. These controllers use the auxiliary observations derived in Section 7 to achieve this control sensorlessly. Collectively, these three controllers determine the form of the control input to the system $v_a(t)$. For the sake of simplicity this voltage command is selected to be a single frequency sinusoid with variable amplitude and frequency based on the following definition:

$$v_a(t) \triangleq V_0(t) \sin \theta_0(t). \tag{109}$$

where $V_0(t) \in \mathbb{R}$ is the amplitude of the waveform and the phase $\theta_0(t) \in \mathbb{R}$ of the waveform is defined as

$$\theta_0(t) \triangleq \int_{t_0}^{t} 2\pi f_0(t). \tag{110}$$

where $f_0(t) \in \mathbb{R}$ is the frequency of the waveform. The form of $\theta_0(t)$ used in (110) is chosen to ensure that the phase is piecewise continuous for step changes in $f_0(t)$.

As can be seen from (109) and (110) the indirect control variables which remain to be defined by the subsequent controllers are the amplitude $V_0(t)$ and frequency, $f_0(t)$ of the voltage command $v_a(t)$. A diagram of the system level control scheme and its interaction with the observers developed previously is shown in Fig. 18.
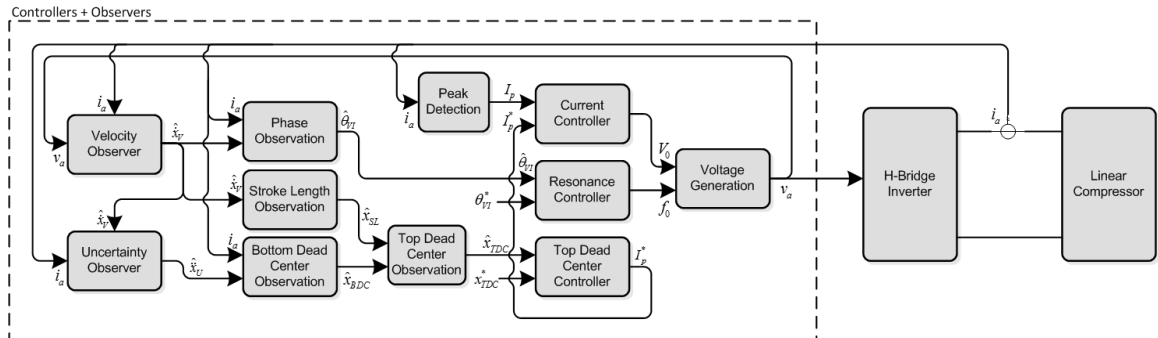

Figure 27. Block diagram of system level sensorless control scheme.

8.1   CURRENT CONTROLLER

The purpose of this controller is to regulate the magnitude of the force being applied to the piston by controlling the motor current per the relationship described in (3). Rather than attempt to achieve full tracking control of the motor current signal, a simpler case is considered in which the peak value of the current is controlled to a desired level. The peak value of the motor current over the previous cycle, denoted as $I_p(t) \in \mathbb{R}$, is here defined as

$$I_p(t) \triangleq \max\{|I(\tau)| : \tau \in (t - T, t]\}. \tag{111}$$

For a given desired peak current $I_p^*(t) \in \mathbb{R}$ a peak current error can be defined as

$$e_I(t) \triangleq I_p^*(t) - I_p(t). \tag{112}$$

The value of the voltage amplitude $V_o(t)$ can be used as a control input for the current controller. A proportional-integral form is chosen for this controller for simplicity and stability and can be defined as

$$V_0(t) = k_P e_I(t) + k_I \int_{t_0}^t e_I(\sigma) d\sigma. \tag{113}$$

8.2   RESONANCE CONTROLLER

The purpose of the resonance controller is to manage the fundamental frequency of the system such that resonance is achieved, thereby maximizing system efficiency. Based on the form of the voltage command defined in (109) it can be shown that the resulting fundamental frequency of all system states will be equal to f_0.

The relative phase of the motor current and piston velocity is used as an indicator of resonance. In this case, the observation of this phase as defined in (104) is used in place of the actual phase. An ideal resonant phase is used as a reference for the controller and is denoted as $\theta_{VI}^* \in \mathbb{R}$. From this a phase error can be defined as

$$e_\theta(t) \triangleq \theta_{VI}^* - \hat{\theta}_{VI}. \tag{114}$$

In the case of single-frequency sinusoidal current and velocity signals this desired phase would be zero to indicate that motor force and velocity were completely in phase. However, since in reality current and velocity will contain multiple harmonics, the phase as defined in (30) will likely be non-zero at resonance.

A search algorithm then utilizes this error signal to make adjustments to the excitation frequency. A piecewise function is used to determine the size of the adjustment denoted as $\Delta f \in \mathbb{R}$ based on the magnitude and sign of the error as shown in (below).

$$\Delta f(e_\theta) \triangleq \begin{cases} \Delta f_1 sgn(e_\theta) & |e_\theta| > e_{\theta_1} \\ \Delta f_2 sgn(e_\theta) & e_{\theta_2} < |e_\theta| \leq e_{\theta_1} \\ \Delta f_3 sgn(e_\theta) & e_{\theta_3} < |e_\theta| \leq e_{\theta_2} \\ 0 & |e_\theta| \leq e_{\theta_3} \end{cases}. \tag{115}$$

where $\Delta f_1, \Delta f_2, \Delta f_3 \in \mathbb{R}^+$ are real positive constants such that $\Delta f_1 > \Delta f_2 > \Delta f_3$, and $e_{\theta_1}, e_{\theta_2}, e_{\theta_3} \in \mathbb{R}^+$ are real positive error threshold constants such that $e_{\theta_1} > e_{\theta_2} > e_{\theta_3}$. Note that when the error is within the smallest threshold the search algorithm no longer makes adjustments to the frequency. This condition is included to prevent unnecessary hunting.

The rate at which these adjustments are made is determined by two conditions. The first condition is that at least T_θ seconds have passed since the most recent adjustment of this controller, where $T_\theta \in \mathbb{R}$ is a pre-determined period of time which is sufficiently long to allow the system dynamics to settle out after an adjustment has been made. The second condition is that the controller has been given priority. The rule set determining this priority is described in a subsequent section.

8.3   TOP DEAD CENTER CONTROLLER

The purpose of the top dead center controller is to control the distance between the piston and the cylinder head. Given a desired top dead center value $x_{TDC}^* \in \mathbb{R}$ a top dead center error signal can be defined as

$$e_x(t) \triangleq x_{TDC}^* - \hat{x}_{TDC}. \tag{116}$$

where $\hat{x}_{TDC}$ could interchangeably be the observation obtained in either Sections 6.5 or 7.4. From this error signal a search algorithm of the same structure as the one described in the previous subsection can then be utilized to make adjustments to the desired peak current. This adjustment, denoted as $\Delta I_p^* \in \mathbb{R}$, is added to the current value of $I_p^*(t)$ and is defined by the following piecewise function:

$$\Delta I_p^*(e_x) \triangleq \begin{cases} \Delta I_1 sgn(e_x) & |e_x| > e_{x_1} \\ \Delta I_2 sgn(e_x) & e_{x_2} < |e_x| \le e_{x_1} \\ \Delta I_3 sgn(e_\theta) & e_{x_3} < |e_x| \le e_{x_2} \\ 0 & |e_x| \le e_{x_3} \end{cases} . \tag{117}$$

where $\Delta I_1, \Delta I_2, \Delta I_3 \in \mathbb{R}^+$ are real positive constants such that $\Delta I_1 > \Delta I_2 > \Delta I_3$, and $e_{x_1}, e_{x_2}, e_{x_3} \in \mathbb{R}^+$ are real positive error threshold constants such that $e_{x_1} > e_{x_2} > e_{x_3}$.

The rate at which these adjustments are made is determined by two conditions, similar to the resonance controller. The first condition is that at least T_x seconds have passed since the most recent adjustment of this controller, where $T_x \in \mathbb{R}$ is a pre-determined period of time which is sufficiently long to allow the system dynamics to settle out after an adjustment has been made. The second condition is that the controller has been given priority. The rule set determining this priority is described in the following section.

8.4   CONTROLLER PRIORITY

Since all three of these controllers are to operate in parallel and the inputs and outputs of each are tied via the system dynamics, special care needs to be taken to ensure stability of the system. In the case of the top dead center controller the situation is even more dire, since its output is a reference to the current controller, making it obvious that care must be taken to restrict the updating of this controller. For this purpose a rule set has been developed to set the priority of these controllers. The goal of this prioritization is to prevent multiple controllers from making large adjustments to their outputs at the same time, which may cause them to fight each other and create instability.

Since the output adjustment of each of the three controllers presented increases with error, we can use their error signals as an indication of how hard the respective controller is working. To facilitate this prioritization, error bounds are established for the current and resonant controller errors defined in (112) and (114), respectively. These error bounds and corresponding Boolean indicators are defined as

$$\beta_I \triangleq \begin{cases} True & |e_I| < e_{I_1} \\ False & |e_I| \ge e_{I_1} \end{cases} \tag{118}$$

$$\beta_\theta \triangleq \begin{cases} True & |e_\theta| < e_{\theta_3} \\ False & |e_\theta| \geq e_{\theta_3} \end{cases} \tag{119}$$

where $e_{I_1} \in \mathbb{R}^+$ is a real positive error threshold constant.

The order of priority established for this system in descending order is current controller, resonant controller, and then top dead center controller. Since the current controller is given highest priority, no restrictions are placed upon its updating, i.e. it updates continuously. As the next highest priority controller, the resonant controller is only allowed to make adjustments to its output when the current error e_I is within its bound, i.e. when β_I is 'True'. As the lowest priority controller, the top dead center controller is only allowed to make adjustments to its output when both the current and resonant controller errors are within their bounds, i.e. when $\beta_I \cdot \beta_\theta$ is 'True'. When one of these conditions is false the corresponding controller output is held at its current value until a 'True' value is detected.

8.5   EXPERIMENTAL RESULTS

The velocity and uncertainty observers defined in (55) and (58) were executed on the FPGA with the parameters and gains listed in Table 3. The resulting $\hat{x}_V(t)$ and $\hat{x}_U(t)$ from these observers were then utilized in real-time to obtain the auxiliary observations described in Section 7. These observations were then utilized to achieve the three-level real-time control described in Section 8 using the parameters and gains listed in Table 3. For this experiment the current controller was run with an initial desired peak current value of $I_p^*(t) = 0.5 \, [A]$ and the resonance controller was run with an initial frequency of $f_0(t) = 56 \, [Hz]$. Based on experimental testing of the compressor efficiency an ideal phase between the positive zero-crossing of the motor current and the piston velocity was identified as $\theta_{VI}^* = 10°$. A fixed desired top dead center value of $x_{TDC}^* = 1 \, [mm]$ was selected for this experiment.

Table 4

Observer and Controller Parameters for Sensorless Overall Control Scheme

Parameter	Value	Units	Parameter	Value	Units
R	6.47	Ω	Δf_1	1	Hz
L	0.318	H	Δf_2	0.1	Hz
α	75.6	N/A	Δf_3	0.01	Hz
M	0.65	kg	e_{θ_1}	20	°
K	72800	N/m	e_{θ_2}	5	°
x_0	6.35	mm	e_{θ_3}	1	°
k_{1_V}	24,000		ΔI_1	0.02	A
k_{2_V}	40,000		ΔI_2	0.01	A
k_{1_U}	4,000		ΔI_3	0.005	A
k_{2_U}	40,000		e_{x_1}	2	mm
k_P	200		e_{x_2}	0.5	mm
k_I	500		e_{x_3}	0.1	mm

With these settings and the system level controller was turned on with the system at rest and allowed to run until all three controllers had reached a steady-state at their respective desired values. The results of the sensorless combined observer/controller hardware implementation are shown in Fig. 28-32. From Fig. 28 and 29 we can see that the current controller remains stable and convergent as the top dead center controller increases the desired peak current. We can also see that the amplitude of the voltage command $V_0(t)$ remains within the limits of the DC link voltage to prevent over-modulation. From the various periods of time in Fig. 28 where the desired peak current remains constant we can see the effect of the controller priority scheme. During these flat periods we can see that the top dead center controller is waiting for the current and resonance controllers to reconverge before making further adjustments to $I_p^*(t)$.

In Fig. 30 and 31 we see that the observed phase $\hat{\theta}_{VI}(t)$ accurately observes the measured phase $\theta_{VI}(t)$ and that the frequency of the voltage command $f_0(t)$ is successfully manipulated to achieve the desired phase. We can see that each time the peak motor current is increased the phase is consistently reduced giving the effect that phase error $e_\theta(t)$ is more positive than negative. However, once steady-state

60

has been achieved from approximately 70 seconds onward, and current adjustments are minor if any, that the phase error is zero-meaned about the desired phase.

In Fig. 32 we see that the observed top dead center $\hat{x}_{TDC}(t)$ accurately observes the measured top dead center $x_{TDC}(t)$ and that the peak current is successfully manipulated to achieve the desired top dead center value. From all of these figures we can see that the rules of priority between the three controllers successfully maintain system-wide stability.
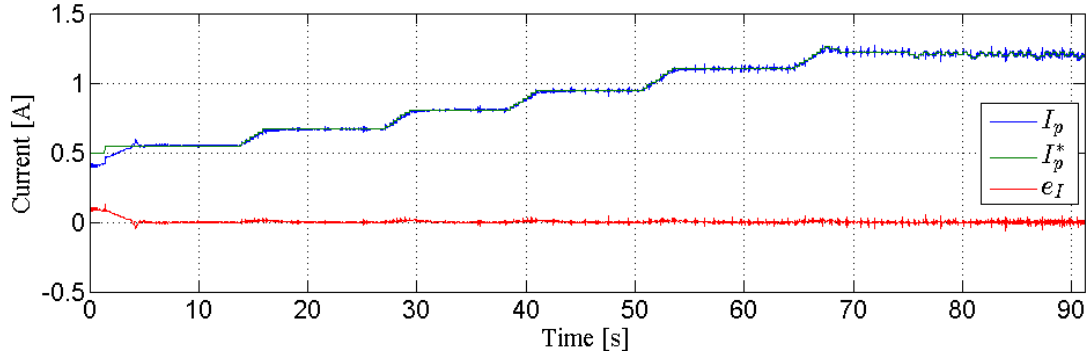

Figure 28. Performance of proportional-integral peak current controller with varying setpoint determined by top dead center controller.
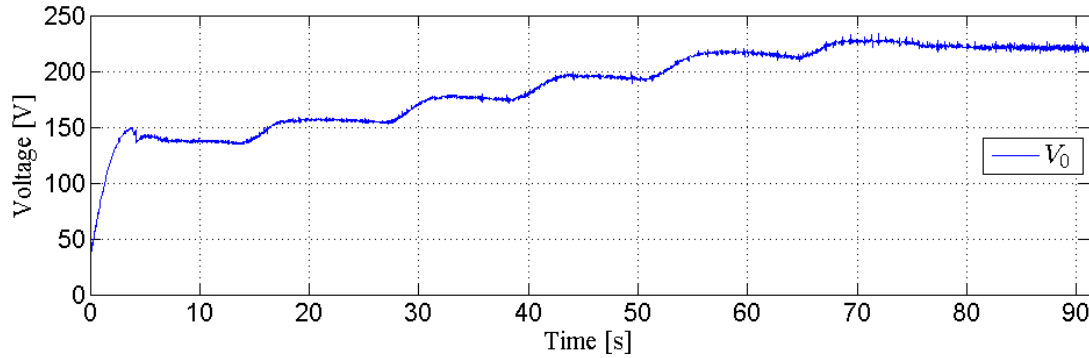
Figure 29. Amplitude $V_0(t)$ of the voltage excitation $v_a(t)$ calculated by the current controller.

<u>Figure 30</u>. Measured and observed phase difference between the piston velocity and measured current with corresponding desired phase.

<u>Figure 31</u>. Frequency $f_0(t)$ of the voltage excitation set by the resonance controller as it attempts to achieve the desired phase shown in Fig. 21.

<u>Figure 32</u>. Measured and observed top dead center with corresponding desired top dead center value.

9 TRACKING CONTROLLERS

9.1 CURRENT CONTROLLER

As a more sophisticated alternative to the regulation current controller described in Section 8.1 a nonlinear current controll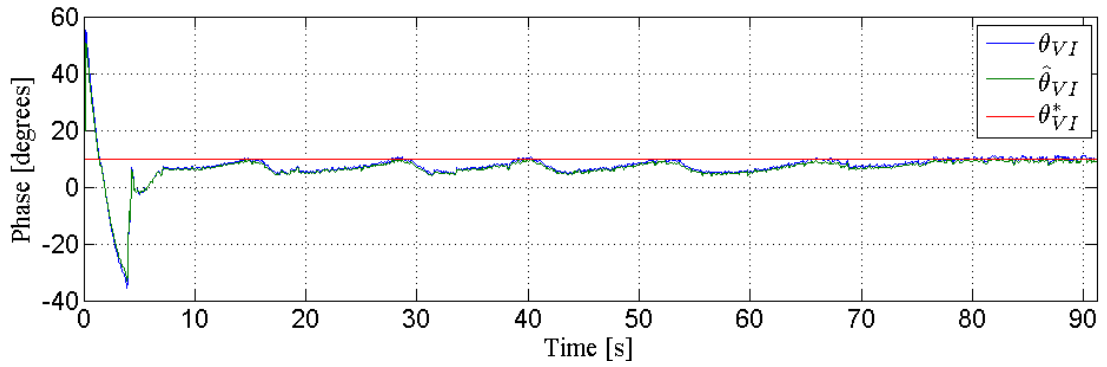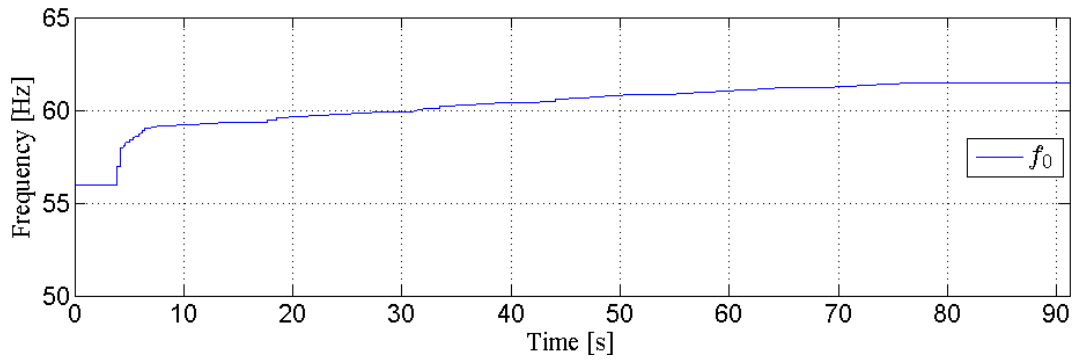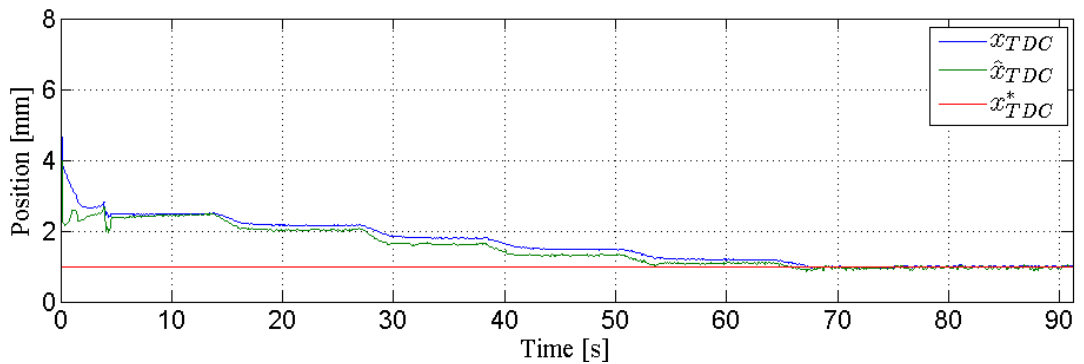er is to be developed for the linear motor to allow for trajectory tracking of the motor current rather than controlling to a single point in the waveform as is currently done in Section 8.1. Expert design of this current trajectory could allow for further increase in the system efficiency.

9.1.1 CONTROL DEVELOPMENT

For a given current trajectory $I_d(t) \in \mathbb{R}$, the designed controller should ensure that $I(t) \to I_d(t)$ as $t \to \infty$. The control input for the system is the motor voltage signal $v_a(t)$. To facilitate the development of the current controller the dynamic equation in (3) can be rewritten as

$$\dot{I} = \frac{1}{L_i}(v_a - R_i I) - f_I \tag{120}$$

where $f_I(t) \in \mathbb{R}$ denotes the uncertain scaled back EMF term $\frac{\alpha}{L_i}\dot{x}$.

The proceeding mathematical analysis necessitates the following set of assumptions (previous assumptions are ignored):

Assumption 1: The signal $v_a(t)$ is assumed to be known and $I(t)$ is assumed to be measurable.

Assumption 2: The signals $x(t), \dot{x}(t), \dot{f}(t), \ddot{f}(t)$ are all assumed to be piecewise continuous and bounded, hence there exist positive bounding constants $\zeta_1, \zeta_2 \in \mathbb{R}^+$ such that $|\dot{f}(t)| < \zeta_1, |\ddot{f}(t)| < \zeta_2$

Assumption 3: The machine parameters L_i, R_i, and α are known *a priori* and are assumed to be constants with respect to time.

Assumption 4: The current trajectory $I_d(t)$ is chosen such that $I_d(t)$ and $\dot{I}_d(t)$ are piecewise continuous and bounded. Through proper design of this trajectory we can ensure tracking of the system resonant frequency.

The following error signals can be defined for the system:

$$e_I \triangleq I_d - I \qquad (121)$$

$$\dot{e}_I = \dot{I}_d - \dot{I}. \qquad (122)$$

Substituting (120) into (122) gives the following open loop error equation:

$$\dot{e}_I = \dot{I}_d - \frac{1}{L_i}(v_a - R_i I) - f_I. \qquad (123)$$

The form of (123) and the subsequent stability analysis motivate the following design for the control input:

$$v_a = L_i(\dot{I}_d - \hat{f}_I) + R_i I \qquad (124)$$

where $\hat{f}(t) \in \mathbb{R}$ is a subsequently designed observer of the back EMF term $f(t)$. An error signal for this observer can be defined as follows:

$$\tilde{f}_I = \hat{f}_I - f_I. \qquad (125)$$

Substituting (124) into (123) and utilizing (125) gives the following closed loop error equation for the system:

$$\dot{e}_I = \tilde{f}_I. \qquad (126)$$

To facilitate the development of the back EMF observer a filtered error signal is defined as follows

$$s_I \triangleq \dot{e}_I + e_I. \qquad (127)$$

From the subsequent stability analysis the following observer is designed:

$$\dot{\hat{f}}_I \triangleq (k_{1_I} + 1)s_I + k_{2_I} sgn(e_I) \qquad (128)$$

where $k_{1_I}, k_{2_I} \in R^+$ are constant gains. As stated in Assumption 1 the signal $\dot{I}(t)$ is not measurable, meaning that $\dot{e}_I(t)$ and therefore $s_I(t)$ are likewise unavailable. A realizable form of the observer can be found by substituting (127) into (128) and integrating both sides of the resulting equation to obtain the following:

$$\hat{f}_I = (k_{1_I} + 1)\left[e_I(t) - e_I(t_0) + \int_{t_0}^{t} e_I(\sigma)d\sigma\right] + k_{2_I} \int_{t_0}^{t} sgn(e_I(\sigma))d\sigma + \hat{f}_I(t_0). \qquad (129)$$

Remark 9.1.1: The stability analysis in the subsequent section proves that the motor current $I(t)$ converges to the current trajectory $I_d(t)$ or in other words that $e(t)$ converges to zero. This stability analysis will also show that $\dot{e}_I(t)$ converges to zero, which per (126) proves that $\hat{f}_I(t)$ converges to $f_I(t)$. From the definition of $f_I(t)$ we can define an observed velocity as

$$\hat{x}_I \triangleq \frac{L_i}{\alpha} \hat{f}_I. \tag{130}$$

9.1.2   STABILITY ANALYSIS

Theorem 9.1.1: The observer defined in (129) ensures that

$$\hat{f}_I(t) \to f_I(t) \quad as \quad t \to \infty \tag{131}$$

provided that the observer gain k_{2_I} is selected to meet the following sufficient condition:

$$k_{2_I} > \zeta_{1_I} + \zeta_{2_I}. \tag{132}$$

Proof: See Appendix.

9.1.3   SIMULATION RESULTS

The simulation model detailed in Section 3 was utilized for this simulation with a switching frequency of 25 [kHz] used for the inverter model. A single frequency sinusoidal current trajectory was chosen for this simulation of the form $I_d(t) = I_0 \sin 2\pi f_0 t \cdot \left(1 - e^{-\beta t^3}\right)$ where $f_0 = 63 \, [Hz], \beta = 75{,}000$ and I_0 is initially 1.4 [A] then undergoes a step change to 2.0 [A] at time $t = 0.119 \, [sec]$. It can be shown that this form fulfills the requirements of Assumption 4. The controller gain $k_{2_I} = 400{,}000$ was selected per the requirements stated in (16) and a value of $k_{1_I} = 7{,}500$ was chosen for the integral gain.

The results of this simulation are shown in Fig. 33-36. Fig. 33 shows the current trajectory $I_d(t)$ along with the actual current $I(t)$. From this and the error signal $e(t)$ in Fig. 34 we can see that the controller is successful in achieving the current control objective and that $I(t) \to I_d(t)$ as $t \to \infty$. The voltage command signal generated by the controller is shown in Fig. 35 along with the corresponding inverter output voltage. Fig. 36 shows an observed velocity signal $\hat{x}_I(t)$ derived from the observed back EMF term $\hat{f}_I(t)$ as shown in (14) versus the actual velocity $\dot{x}(t)$. Since it has been proven through the stability analysis that $\hat{f}_I(t) \to f_I(t)$ as $t \to \infty$, it can be shown that likewise that $\hat{x}_I(t)$ converges to $\dot{x}(t)$. This statement is further validated by the results shown in Fig. 36.
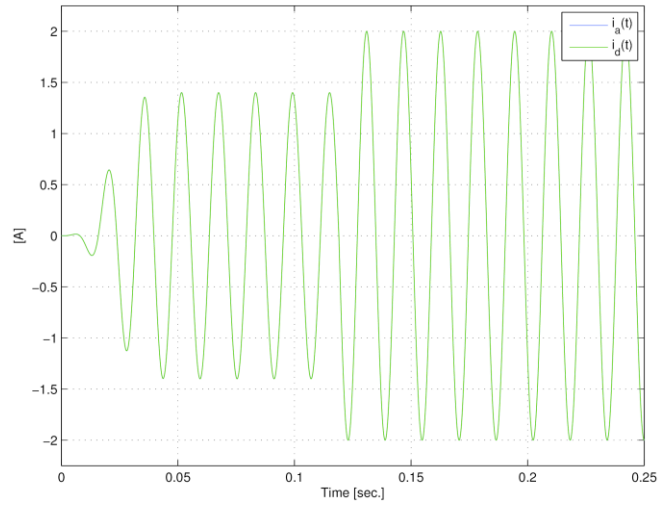
Figure 33. Convergence of actual current $I(t)$ to the current trajectory $I_d(t)$.
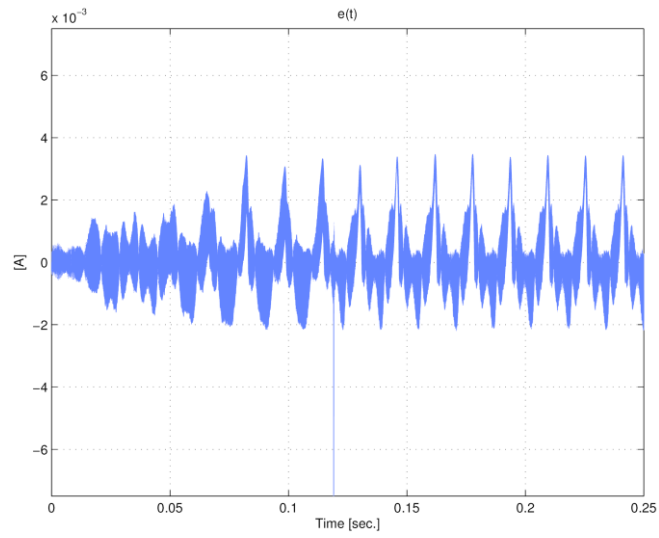

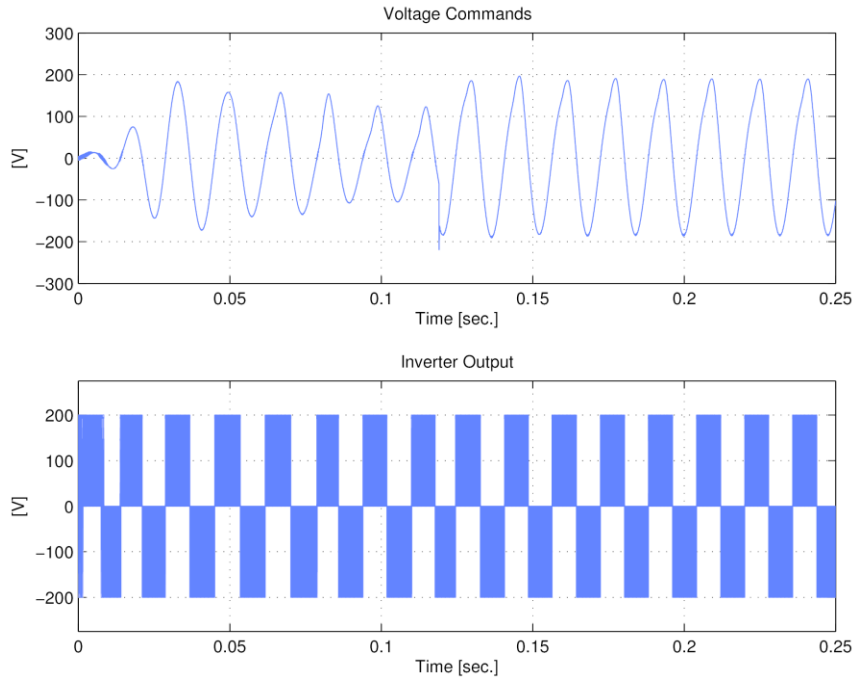Figure 34. Convergence of current error $e_I(t)$ to zero.

Figure 35. Controller voltage command $v_a(t)$ and corresponding H-bridge inverter output.
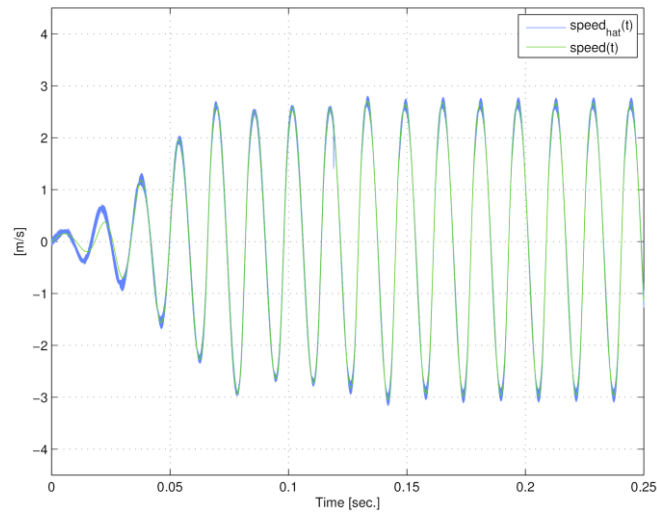
Figure 36. Comparison of observed velocity $\hat{\dot{x}}_l(t)$ with actual velocity $\dot{x}(t)$.

CONCLUSION

A series of estimators, observers, and control schemes have been developed to allow for a sensorless system level control scheme which is capable of achieving efficient stroke control of a linear vapor compressor. The system level control has been implemented using three individual controllers operating in parallel with a simple rule set preventing fighting between them. The information needed for the operation of these controllers has been derived sensorlessly from a pair of Lyapunov stable nonlinear observers. The first of these is a velocity observer, which is used to do determine the relative phase of the motor current and piston velocity, an indicator of system efficiency. The second is a position and pressure observer which uses this velocity signal to observe the absolute position of the piston along with the system pressures. Both of these observers rely on accurate knowledge of the machine parameters which have been obtained through a pair of adaptive least-squares estimators. Analysis and experimental results have been provided for validation of each of the proposed algorithms, demonstrating successful and accurate operation.

REFERENCES

[1]   R. L. Unger, "Linear compressors for non-CFC refrigeration," in *Int. Appl. Tech. Conf.*, West Lafayette, IN, May 1996, pp. 373-380.

[2]   R. L. Unger, "Linear compressors for clean and specialty gases," in *Int. Compress. Eng. Conf.*, West LaFayette, IN, Jan. 1998, pp. 51-56.

[3]   R. W. Redlich, R. Unger and N. van der Walt, "Linear compressors: motor configuration, modulation and systems," in *Int. Compress. Eng. Conf.*, West Lafayette, IN, July 1996, pp. 341-346.

[4]   Y.-P. Yang and W.-T. Chen, "Dual stroke and phase control and system identification of linear compressor of a split-Stirling cryocooler," *Asian J. of Control,* vol. 1, no. 2, pp. 116-121, June 1999.

[5]   B. J. Huang and Y. C. Chen, "System dynamics and control of a linear compressor for stroke and frequency adjustment," *J. of Dyn. Syst., Meas., and Control,* vol. 124, no. 1, pp. 176-182, Feb. 2001.

[6]   R. W. Redlich, "Method and apparatus for measuring piston position in a free piston compressor". U.S. Patent 5342176, 30 August 1994.

[7]   J. Zhang, Y. Chang and Z. Xing, "Study on self-sensor of linear moving magnet compressor's piston stroke," *IEEE Sensors J.,* vol. 9, no. 2, pp. 154-158, Feb. 2009.

[8]   J. Sung, C. Lee, G. Kim, T. Lipo, C. Won and S. Choi, "Sensorless control for linear compressors," *Int. J. of Appl. Electromagn. and Mech.,* vol. 24, no. 3-4, pp. 273-286, Mar. 2006.

[9]   T.-W. Chun, J.-R. Ahn, J.-Y. You and C.-W. Lee, "Analysis and control for linear compressor system driven by PWM inverter," in *30th Annu. Conf. IEEE Ind. Electron. Soc.*, Busan, Korea, pp. 263-267, Nov. 2004.

[10] J.-K. Son, T.-W. Chun, H.-H. Lee, H.-G. Kim and E.-C. Nho, "Method of estimating precise piston stroke of linear compressor driven by PWM inverter," in *16th Int. Power Electron. and Motion Control Conf. and Expo.*, Antalya, Turkey, Sept. 2014, pp. 673-678.

[11] Z. Lin, J. Wang and D. Howe, "A resonant frequency tracking technique for linear vapor compressors," in *Elect. Mach. & Drives Conf.*, Antalya, Turkey, May 2007, pp. 370-375.

[12] T.-W. Chun, J.-R. Ahn, H.-H. Lee, H.-G. Kim and E.-C. Nho, "A novel strategy of efficiency control for a linear compressor system driven by a PWM converter," *IEEE Trans. Ind. Electron.,* vol. 55, no. 1, pp. 296-301, Jan. 2008.

[13] S.-B. Yang, "Linear compressor control circuit to control frequency based on the piston position of the linear compressor". United States of America Patent 5947693, 7 September 1999.

[14] M. Yoshida, S. Hasegawa and M. Ueda, "Driving apparatus of a linear compressor". United States of America Patent 6832898, 21 December 2004.

[15] B.-J. Choi and e. al, "Linear compressor". United States of America Patent 7,816,873, 9 March 2009.

[16] Z. Lin, J. Wang and D. Howe, "A learning feed-forward current controller for linear reciprocating vapor compressors," *IEEE Trans. Ind. Electron.,* vol. 58, no. 8, pp. 3383-3390, Aug. 2011.

[17] Y. Zhu and P. Pagilla, "Adaptive Estimation of Time-Varying Parameters in Linear Systems," in *Proc. Amer. Control Conf.*, Denver, CO, 2003, pp. 4167-4172.

[18] S. Sastry and M. Bodson, Adaptive Control: Stability, Convergence, and Robustness, Englewood Cliffs, NJ: Prentice Hall Inc., 1989.

[19] M. McIntyre, T. Burg, D. Dawson and B. Xian, "Adaptive state of charge (SOC) estimator for a battery," in *Proc. Amer. Control Conf.*, Minneapolis, MN, 2006, pp. 5740-5744.

[20] M. Salah, M. McIntyre, D. Dawson and J. Wagner, "Sensing of the time-varying angular rate for MEMS Z-axis gyrsocopes," *IEEE Trans. Mechatron.,* vol. 20, no. 6, pp. 720-727, 2010.

[21] E. Tatlicioglu, M. McIntyre, D. Dawson and I. Walker, "Adaptive Nonlinear Tracking Control of Kinematically Redundant Robot Manipulators with Sub-Task Extensions," in *44th IEEE Conf. on Decision and Control*, Seville, 2005.

[22] D. W. Hart, "Inverters," in *Power Electronics*, New York, McGraw-Hill, 2011, ch. 8, sec. 10, pp. 358-359.

[23] J. Slotine and W. Li, Applied Nonlinear Control, Englewood Cliffs, NJ: Prentice Hall, 1991.

[24] G.-S. Choe and K.-J. Kim, "Analysis of nonlinear dynamics in a linear compressor," *JSME Int. J.,* vol. 43, no. 3, pp. 545-552, Aug. 2000.

[25] J. Latham, M. L. McIntyre and M. Mohebbi, "Parameter estimation and a series of nonlinear observers for the system dynamics of a linear vapor compressor," *IEEE Trans. Ind. Electron.,* vol. 63, no. 11, pp. 6736-6744, Nov. 2016.

APPENDIX

Remark A.1: We can see that a similar RISE based observer methodology was used to develop velocity, acceleration, and gas force observers in Sections VI.A, VI.B, VI.D respectively as well as the observer-based current controller in Section IX.A. Given that the closed loop error dynamics and the form of the observers defined in (33) and (47) are identical a single stability analysis is given for all three systems for the sake of brevity. The subscript i used in the subsequent analysis may be replaced with a $V, U, F,$ or I to refer to terms in the velocity observer, acceleration observer, gas force observer, or current controller development, respectively.

The relevant error definitions, closed loop dynamics, and observer definitions are repeated here for use in the subsequent analysis. Corresponding equations can be found in the respective development sections.

$$\tilde{f}_i \triangleq f_i - \hat{f}_i \tag{133}$$

$$\dot{e}_i = \tilde{f}_i \tag{134}$$

$$s_i \triangleq \dot{e}_i + e_i \tag{135}$$

$$\dot{\hat{f}}_i \triangleq \left(k_{1_i} + 1\right)s_i + k_{2_i} sgn(e_i) \tag{136}$$

Corresponding equations can be found in the development sections mentioned.

Theorem A1: The observer defined in (136) ensures that

$$\hat{f}_i(t) \to f_i(t) \quad as \quad t \to \infty \tag{137}$$

provided that the observer gain k_{2_i} is selected to meet the following sufficient condition:

$$k_{2_i} > \zeta_{1_i} + \zeta_{2_i}. \tag{138}$$

Proof: To prove that $\hat{f}_i(t) \to f_i(t)$ as $t \to \infty,$ a nonnegative Lyapunov function $V_i(t) \in \mathbb{R}$ is defined for the observer as

$$V_i \triangleq \frac{1}{2}e_i{}^2 + \frac{1}{2}s_i{}^2 \tag{139}$$

where $e_i(t)$ is the error of the respective controller/observer and $s_i(t)$ is the corresponding filtered error defined in (135). Further analysis will show that the form of $\hat{f}_i(t)$ presented in (136) ensures that $\dot{V}_i(t)$ is negative definite for all $e_i(t)$ and $s_i(t)$. The time derivative of (139) is taken and can be written as

$$\dot{V}_i = e_i \dot{e}_i + s_i \dot{s}_i. \tag{140}$$

An expression for $\dot{s}_i(t)$ can be written by taking the time derivative of (135), and substituting the time derivatives of (133) and (134) to obtain the following:

$$\dot{s}_i = \dot{f}_i - \dot{\hat{f}}_i + \dot{e}_i. \tag{141}$$

Solving (135) for $\dot{e}_i(t)$ an expression is obtained which can be substituted along with (141) into (140) with the following result:

$$\dot{V}_i = -e_i{}^2 + s_i{}^2 + s_i(\dot{f}_i - \dot{\hat{f}}_i). \tag{142}$$

Substituting (135) and (136) into (142), after simplifying the result can be written as

$$\dot{V}_i(t) = -e_i{}^2 - k_{1_i} s_i{}^2 + \dot{e}_i \dot{f}_i - k_{2_i} \dot{e}_i sgn(e_i) + e_i(\dot{f}_i - k_{2_i} sgn(e_i)). \tag{143}$$

The integral of (143) from t_0 to t can be expressed as

$$V_i(t) = V_i(t_0) - \int_{t_0}^{t} e_i{}^2(\sigma) d\sigma - k_{1_i} \int_{t_0}^{t} s_i{}^2(\sigma) d\sigma + \int_{t_0}^{t} \dot{e}_i(\sigma) \dot{f}_i(\sigma) d\sigma$$

$$- k_{2_i} \int_{t_0}^{t} \dot{e}_i(\sigma) sgn(e_i(\sigma)) d\sigma + \int_{t_0}^{t} e_i(\sigma)[\dot{f}_i(\sigma) - k_{2_i} sgn(e_i(\sigma))] d\sigma. \tag{144}$$

After integrating the fourth term of the right-hand side of (144) by parts and the fifth term with respect to time and rearranging terms the following expression is obtained for $V_i(t)$:

$$V_i(t) = V_i(t_0) - \int_{t_0}^{t} e_i{}^2(\sigma) d\sigma - k_{1_i} \int_{t_0}^{t} s_i{}^2(\sigma) d\sigma + e_i(t) \dot{f}_i(t) - e_i(t_0) \dot{f}_i(t_0)$$

$$- k_{2_i} |e_i(t)| + k_{2_i} |e_i(t_0)| + \int_{t_0}^{t} e_i(\sigma)[\dot{f}_i(\sigma) - \ddot{f}_i(\sigma) - k_{2_i} sgn(e_i(\sigma))] d\sigma. \tag{145}$$

Provided that k_{2_i} is selected according to (138), the fourth and sixth terms of the right-hand side of (145) can be combined and upper bounded to zero. Similarly, the eighth term can also be upper bounded to zero. After applying these upper bounds to (145), $V_i(t)$ can be upper bounded as follows:

$$V_i(t) \leq - \int_{t_0}^{t} |e_i(\sigma)|^2 d\sigma - k_{1_i} \int_{t_0}^{t} |s_i(\sigma)|^2 d\sigma + C_i. \tag{146}$$

where $C_i \triangleq V_i(t_0) - e_i(t_0)(\dot{f}_i(t_0) - k_{2_i} sgn(e_i(t_0)))$ is a bounding constant.

From the structure of (139) and (146) and the definition of C_i it is proven that $V_i(t) \in \mathcal{L}_\infty$; hence

$s_i(t), e_i(t) \in \mathcal{L}_\infty$. Since $s_i(t), e_i(t) \in \mathcal{L}_\infty$, from (135) and (136) it is clear that $\dot{e}_i(t), \dot{\hat{f}}_i(t) \in \mathcal{L}_\infty$. Since

$\dot{f}_I(t), \dot{\hat{f}}_i(t), s_i(t), e_i(t)$ and $\dot{e}_i(t) \in \mathcal{L}_\infty$, it is clear from (141) that $\dot{s}_i(t) \in \mathcal{L}_\infty$. The inequality defined by

(146) can be used to prove that $s_i(t), e_i(t) \in \mathcal{L}_2$. Since $s_i(t), e_i(t), \dot{s}_i(t), \dot{e}_i(t) \in \mathcal{L}_\infty$ and $s_i(t), e_i(t) \in$

$\mathcal{L}_2$, then Barbalat's lemma can be used to prove that $s_i(t)$ and $e_i(t) \to 0$ as $t \to \infty$. Since $s_i(t) \to 0$ as $t \to$

∞, (135) can be used to show that $\dot{e}_i(t) \to 0$ as $t \to \infty$ as well. From this fact and (134) we see that $\hat{f}_i(t) \to$

$f_i(t)$ thus completing the proof of Theorem A1.

CURRICULUM VITAE

NAME: Joseph Wilson Latham

ADDRESS: Department of Electrical and Computer Engineering
                    W. S. Speed Hall, Rm. 207
                    University of Louisville
                    Louisville, KY 40292

DOB: Greenville, Kentucky – August 19, 1988

EDUCATION
& TRAINING: B.S., Electrical Engineering
                    Western Kentucky University
                    2006-2012

                    M.S., Electrical and Computer Engineering
                    University of Louisville
                    2013-2014

                    Ph.D., Electrical Engineering
                    University of Louisville
                    2014-2017

AWARDS: Outstanding Graduate Student
                    Dept. of Electrical and Computer Engineering
                    University of Louisville
                    2016-2017

                    University Fellowship
                    University of Louisville
                    2014-2016

                    Award of Excellence Scholarship
                    Western Kentucky University
                    2006-2007, 2010-2012

PUBLICATIONS:

   J. Latham, M. L. McIntyre and M. Mohebbi, "Sensorless resonance-tracking and stroke control of a

linear vapor compressor via nonlinear observers," *IEEE Trans. Ind. Electron., under review,* 2016.

   J. Latham, M. L. McIntyre and M. Mohebbi, "Parameter estimation and a series of nonlinear

observers for the system dynamics of a linear vapor compressor," *IEEE Trans. Ind. Electron.,* vol. 63, no. 11, pp. 6736-6744, Nov. 2016.

M. L. McIntyre, W. Burke, J. Latham and J. Graham, "Smart appliances energy study," *Int. J. of Comput. and their Applicat.,* vol. 21, no. 3, pp. 142-150, 2014.

J. Latham, M. L. McIntyre and M. Mohebbi, "Nonlinear adaptive current control for linear vapor compressors," in *2016 IEEE Int. Conf. on Automat. Sci. and Eng. (CASE)*, Fort Worth, TX, pp. 1157-1162, Aug. 2016.

M. L. McIntyre, M. Mohebbi and J. Latham, "Nonlinear current observer for backstepping control of buck-type converters," in *IEEE 16th Workshop on Control and Modeling for Power Electron. (COMPEL)*, Vancouver, pp. 1-7, July 2015.

M. Mohebbi, M. L. McIntyre and J. Latham, "Energy efficient DC to AC power conversion using advanced controllers and novel voltage trajectories," in *IEEE 16th Workshop on Control and Modeling for Power Electron. (COMPEL)*, Vancouver, pp. 1-8, July 2015.

M. Mohebbi, M. L. McIntyre and J. Latham, "Vehicle to grid utilizing a backstepping controller for bidirectional full-bridge converter and five-level active neutral point inverter," in *IEEE 16th Workshop on Control and Modeling for Power Electron. (COMPEL)*, Vancouver, pp. 1-7, July 2015.

M. Elliot, M. L. McIntyre and J. Latham, "Partial shading abatement through cell level inverter system topology," in *IEEE 42nd Photovoltaic Specialist Conf. (PVSC)*, New Orleans, pp. 1-5, June 2015.

M. L. McIntyre, W. Burke, J. Latham and J. Graham, "Energy usage patterns in fielded smart appliances," in *29th Int. Conf. on Comput. and their Applicat. (CATA)*, Las Vegas, pp. 181-188, March 2014.

M. L. McIntyre, M. Schoen and L. J., "Simplified adaptive backstepping control of Buck DC:DC converter with unknown load," in *IEEE 14th Workshop on Control and Modeling for Power Electron. (COMPEL)*, Salt Lake City, pp. 1-7, June 2013.

M. L. McIntyre, M. Schoen and J. Latham, "Backstepping control of a capacitance-less photovoltaic power converter with maximum power point tracking," in *IEEE 39th Photovoltaic Specialist Conf. (PVSC)*,

Tampa, pp. 2908-2913, June 2013.

PATENTS:

J. W. Latham, M. L. McIntyre, G. Hahn and S. Kusumba, "A method for operating a linear compressor". U.S. Patent Docket Number 280752-1/GECA-1135, filed Nov. 2015, (unique claims for system level control scheme).

J. W. Latham and M. L. McIntyre, "A method for operating a linear compressor". U.S. Patent App. #14/607,365, filed Jan. 2015, (unique claims for top dead center observation).

J. W. Latham and M. L. McIntyre, "A method for operating a linear compressor". U.S. Patent App. #14/607,347, filed Jan. 2015, (unique claims for stroke length observation).

J. W. Latham and M. L. McIntyre, "A method for operating a linear compressor". U.S. Patent App. #14/607,374, filed Jan. 2015, (unique claims for parameter estimation).

INVITED PRESENTATIONS:

"A backstepping controller for voltage source inverter with inductor current and output current observers," in Power and Energy Conf. at Illinois (PECI), Champaign, 2017.

"Output feedback control of a single phase voltage source inverter utilizing a variable structure observer," in American Controls Conf., Seattle, 2017.